UiO : Department of Geosciences
University of Oslo

Halo photography: retrieval of ice crystal properties in Arctic cirrus clouds

Ingrid Lundhaug

Master's Thesis, Spring 2023

Abstract

Halo displays are optical phenomena in the sky, produced by the presence of thin cirrus clouds. These clouds consist of non-spherical ice crystals, which interact with solar and terrestrial radiation and affect the Earth's climate. Their ice crystals vary in size and shape depending on their formation and the surrounding atmospheric conditions. The shapes can vary from hexagonal plates and columns to structures such as bullet rosettes and aggregates. Depending on the ice crystal's orientation and shape, the halo displays can have different appearances. Current remote sensing techniques struggle to provide information on ice crystal shapes. As the radiative properties of cirrus clouds are also dependent on their ice crystal shapes, observations of halo displays can be a valuable tool to add to other remote sensing techniques. In consequence, our understanding of the microphysics of cirrus clouds can be improved and, ultimately, better estimates of their radiative properties can be provided.

In this thesis, a digital camera was characterized and radiometrically calibrated to quantify the radiance distribution from images of halo displays. The capabilities of the camera are demonstrated at an Arctic halo event on 22 February 2023. According to the observations and forward modeling with the radiative transfer model libRadtran, the cirrus clouds on that day consisted predominantly of smooth plates. Collocated in-situ observations from a research aircraft also identified mainly plates in the clouds. These findings show that halo observations can be a valuable tool for characterizing ice crystal properties even under low Sun conditions in the Arctic. Further long-term observations of halo displays are needed for a comprehensive statistical study of the ice crystal properties in Arctic cirrus clouds.

Sammendrag

Haloformasjoner er optiske fenomener som kan sees på himmelen. Disse fenomenene oppstår på grunn av sollys som skinner igjennom tynne cirrusskyer. Cirrusskyer består av iskrystaller med ujevne former, i motsetning til sfæriske vanndråper. Iskrystallene sprer og reflekterer innkommende solstråling, i tillegg til å absorbere og emittere infrarød stråling fra jordoverflaten. For å estimere effekten cirrusskyer har på strålingsbudsjettet, må egenskapene til iskrystallene karakteriseres. Iskrystaller kan variere i størrelse og form avhengig av hvordan de er formert, og de nærliggende atmosfæriske forholdene. Formen kan variere fra sekskantede plater til kolonner, med flere underkategorier. Haloformasjoner vil kunne ha forskjellige utseende på grunn av formen og orienteringen til iskrystallene. Dagens fjernmålingsmetoder av cirrusskyer har vanskeligheter for å karakterisere formen på iskrystaller. Siden formen på iskrystallene er en av faktorene som påvirker strålingsegenskapene til cirrusskyer, vil observasjoner av haloformasjoner kunne være et viktig tillegg til andre fjernmålingsmetoder. I denne oppgaven vil vi kategorisere og kalibrere et digitalt kamera for å estimere strålingsfordelingen i bilder av haloformasjoner. Denne evnen til kameraet vil demonstreres for en haloformasjon den 22. februar 2023 for et Arktisk område. I følge observasjonene og simuleringer fra strålingsmodellen, libRadtran, bestod cirrusskyen hovedsakelig av glatte iskrystallplater. Samlokaliserte observasjoner av cirrusskyen fra et forskningskfly identifiserte også hovedsakelig plater. Disse funnene viser at observasjoner av haloformasjoner kan karakterisere egenskaper til iskrystaller, selv ved lave solforhold som i Arktiske strøk. For en utfyllende statistisk studie av egenskapene til iskrystaller i Arktiske cirrusskyer, vil langtidsobservasjoner av haloformasjoner være nødvendig.

Acknowledgements

First of all, I would like to express my gratefulness to my main supervisor, Tim Carlsen, for making this thesis possible and for introducing me to the field of remote sensing of Arctic cirrus clouds. Your guidance has been extremely valuable, and I am incredibly grateful for the time you have dedicated to me. Your availability, positive attitude, and willingness to help have inspired me throughout this process. I have learned so much from you about the scientific process, from collecting data to creating scientific content. In addition, I really apricate all your help with the radiative transfer simulations, so thank you!

I would also like to thank the UiO group, MC2, with Trude Storelvmo at the forefront, for interesting talks, and for welcoming me into the scientific community. Thank you to Rob David and Tim Carlsen for organizing a successful field campaign in Andenes. I enjoyed testing the HaloCam in the field and learning about other instruments used for meteorological measurements. I am also grateful to campaign members during my campaign time, Britta Schäfer, and fellow master student Stian, for making the experience even more enjoyable.

I am thankful for my fellow master students and the supportive environment we created in our study room. Despite our small numbers, I'm grateful for great friendships, and the help we got from each other. I would like to extend my gratitude to Sigrid and Anne Gro for always being there to cheer me up.

I would like to thank my parents for always supporting me, and my friend, Emilia, for taking care of my creative side during this process. Finally, I want to thank Erlend for being you, and always lifting me up and making me smile.

Contents

List of Figures

List of Tables

CHAPTER 1

Introduction

1.1 Motivation

Cirrus clouds have global fractional coverage of 23%. The fractional coverage over Arctic regions can be up to 20%-45%. This globally common cloud type as shown in figure 1.1, significantly modifies the Earth's radiation budget (Heymsfield et al., 2017). Their impact on radiation occurs as they scatter solar radiation and absorb and emit thermal infrared radiation from the surface. Cirrus clouds have the potential to either cool or warm the climate depending on if they scatter more incoming radiation back to space, or trap more thermal radiation in the Earth system. To determine the effects of cirrus clouds on the radiative budget, their optical thickness, the effective radius of their ice crystals, and the ice crystal's shape and orientation need to be accounted for (L. Forster et al., 2017). Ice crystals in cirrus clouds have a broad variation with sizes ranging from less than 10 μm to some thousands of micrometers (Baran, 2004), and with typical shapes of hexagonal solid or hollow columns, plates, bullet rosettes, or aggregates (Heymsfield et al., 2017).

As global warming proceeds, clouds in general will contribute to a positive feedback, which amplifies the warming of the climate system. This feedback is stronger with lower uncertainty in the Sixth Assessment Report (AR6) due to a better understanding of cloud processes (Zelinka et al., 2020). Still, cloud feedbacks are the largest uncertainty in global climate models (P. Forster et al., 2021). Hence, further knowledge regarding cirrus clouds radiative properties, including ice crystal shape and orientation, is needed to improve estimates of climate sensitivity in global climate models.

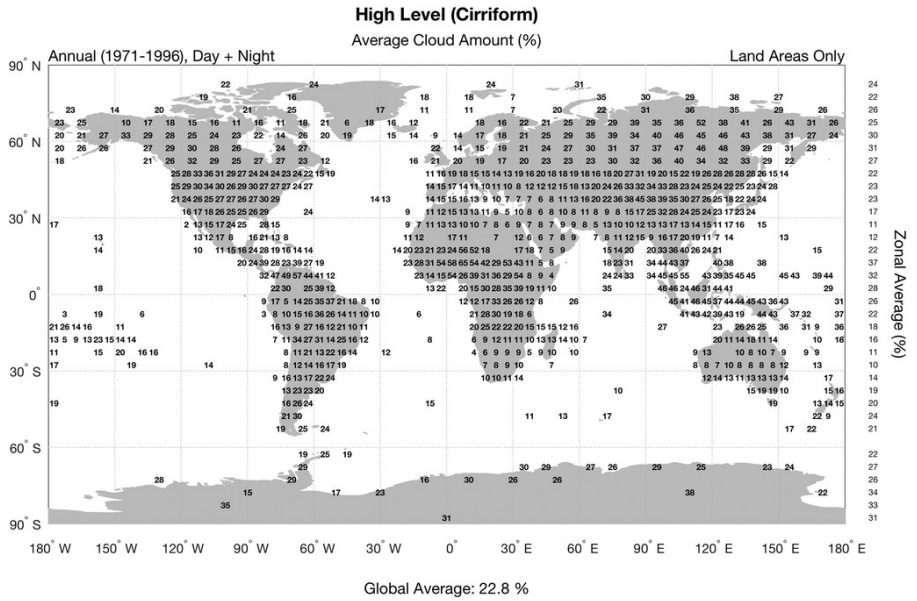

Figure 1.1: Global fractional cirrus cloud coverage over the period of 1971-1996. Figure from Heymsfield et al., 2017.

Remote sensing of cirrus clouds is an important tool for the retrieval of ice crystal microphysical parameters. Satellite observations are a common remote sensing technique, but lack information on ice crystal shape. Consequently, the accuracy of simulated radiative properties of cirrus clouds is limited (Minnis et al., 1998). Hence, further knowledge of cirrus clouds ice crystal shapes is necessary to improve the simulations of their radiance fields.

Halo displays are bright circles, spots, and arcs around the sun, produced by refraction and reflection of sunlight due to prism-shaped ice crystals in thin cirrus clouds (L. Forster et al., 2017; L. Forster et al., 2020; Wang, 2013). The most common halo is the 22° halo, which is formed when photons are scattered in a forward direction between two of the rectangular faces of the ice crystal (L. Forster et al., 2017). The solar ray will then have a shift in direction of 22° from the incident ray. The bending of light through the ice crystal is a single-scattering process. Information of ice crystals single-scattering properties can be used to describe ice crystal size, shape, and surface roughness (Forster and Mayer, 2022; Baran, 2004). Consequently, halo displays can provide information on the single-scattering properties of ice crystals, hence improving our understanding of the radiative properties of cirrus clouds.

Halo display studies on single-scattering properties of cirrus clouds have earlier been performed by Forster (2017); L. Forster et al. (2017); L. Forster et al. (2020); Forster and Mayer (2022), with focus on mid-latitude cirrus clouds. This thesis focuses on the single-scattering properties of Arctic cirrus clouds, as the Arctic air surface temperature has increased more than twice as fast as the global average in the last 20 years (Meredith et al., 2019). Previous studies from Korolev et al. (1999) have also retrieved ice crystal shapes in the Arctic, but by using in-situ measurements. The Arctic is linked with the entire Earth through oceans and the atmosphere, thereby it is considered a key component of the global climate system. Thereby, the warming of the Arctic has crucial consequences for further climate changes for the rest of the Earth, affecting its people (Meredith et al., 2019). This rapid warming is a known phenomenon called Arctic amplification. The main drivers of Arctic amplification are the surface albedo feedback due to the loss of snow and sea ice, the poleward heat transport from low latitudes in the ocean and atmosphere, which is more efficient than the heat transport equatorward, and the increasing occurrence of moist air mass intrusions affecting the lapse-rate, water vapor, and cloud feedbacks (Taylor et al., 2022). Present climate models struggle to represent the rapid warming in the Artic to its fullest extent (Chylek et al., 2022). As high-latitude cirrus clouds are composed of fewer and larger ice crystals than mid-latitude cirrus clouds due to cleaner air (De La Torre Castro et al., 2023), the single-scattering properties are different. Studying these properties of Arctic cirrus clouds can therefore improve estimates of Arctic amplification.

1.2 Project description

A digital camera, referred to as HaloCam, was characterized and calibrated to measure halo displays. This includes a geometric calibration to relate the image pixels to spherical coordinates. The geometric calibration introduces a viewing azimuth and zenith angle for each image pixel. Moreover, since halo displays are a single-scattering phenomenon, the viewing zenith angle is directly linked to the scattering angle of ice crystals. A radiometric calibration was also performed to relate the pixels to a physical quantity of radiance. The characterization of the camera includes calculations of the linearity, dark current, electronic noise,

and relative spectral response of the image sensor, which are needed for the radiometric calibration. To test the capabilities of the camera, measurements from a pilot study at Andenes in northern Norway were analyzed.

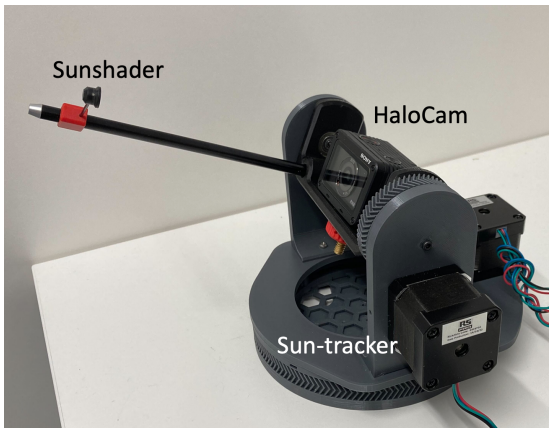

Figure 1.2: The HaloCam with a sunshader in front of the lens to block the sun, mounted on a sun-tracker.

The aim of this thesis is to characterize and calibrate a camera, to look into single-scattering properties of ice crystals in Arctic cirrus clouds. Accordingly, the ice crystal properties can be provided. The principal method for retrieving this information follows the approach as in Forster (2017). A digital camera (HaloCam) is used to take pictures of halo displays. To optimize the possible signal of the bright halo, and avoid stray light, a sunshader was mounted in front of the lens to cover the sun. For this thesis, a 22° halo was used to characterize the ice crystal shape of a cirrus cloud on 22 February 2023. After calibrating the camera, the intensity of the 22° halo was used to compute radiance distribution dependent on the scattering angle of the ice crystals. This can provide information on ice crystal size and shape from the bright part of the halo, as well as the cirrus cloud optical depth from the radiance distribution including the surrounding darker part around the halo (Forster and Mayer, 2022). The radiance distribution is compared to radiative transfer simulations, using the software package; libRadtran. Hence, a complete characterization of ice crystal shapes including surface roughness is provided. To validate the result of the ice crystal shape, the halo observation was compared to collocated airborne measurements of the cirrus clouds.

1.3 Outline

The rest of the text is organized as follows:

Chapter 2 presents a theoretical background needed as a basis for the results and discussion in this thesis.

Chapter 3 demonstrates how the camera was calibrated. The chapter also includes calculations for the characterization and calibrations of the camera, which are required for processing images of halo displays.

Chapter 4 features an overview of the Arctic Halo case study on 22 February 2023. Moreover, the radiative transfer simulations are described, and the resulting observed and simulated radiance distributions are presented.

Chapter 5 discusses the similarities between the observed and simulated radiance distributions, to determine an ice crystal shape that dominates in the cirrus cloud. In addition, the uncertainties of this study are presented.

Chapter 6 features a summary and the conclusion of this thesis. Finally, future work regarding Arctic halo observations is summarized in an outlook.

CHAPTER 2

Background

This chapter introduces a theoretical background for this thesis, to get a better understanding of how halo displays are linked to cirrus clouds, and how cirrus clouds affect the Earth's radiation budget. The first section of this chapter presents the formation of cirrus clouds and ice crystals, as well as microphysical properties of ice crystals. Since ice crystals in cirrus clouds efficiently absorb and re-emit infrared radiation (Lamb and Verlinde, 2011), the next section will present the cirrus clouds effect on the radiation budget including the radiative transfer equation. The last section will then explain the optical phenomena of halo displays, and the formation of the 22° and 46° halos.

2.1 Cirrus clouds and ice crystals

2.1.1 Formation of Cirrus clouds

Cirrus clouds are high-level clouds, at altitudes greater than 6 km (Wang, 2013). They are classified as ice clouds and consist of non-spherical ice crystals. The temperature has to be lower than -43 C° for the clouds to consist completely of ice (Guignard et al., 2012). There are three main types of cirrus clouds: cirrus, cirrocumulus, and cirrostratus, which are illustrated in figure 2.1. Cirrus clouds have a wispy and streaky appearance, caused by wind shear at cloud level (Wang, 2013). Cirrocumulus clouds have a more wavy and patchy structure. Cirrostratus clouds form as a more or less uniform thin layer and are often seen together with a halo.

Figure 2.1: Cirrus, cirrocumulus, and cirrostratus illustrated from left to right. Collected from (WMO, 2017).

In general, clouds form when water vapor in a cooling, moist air parcel gets supersaturated with respect to liquid water or ice. Typical mechanisms that force an air parcel to supersaturation are lifting of the air parcel, contamination of particles that make it easier for water vapor to condense on, or radiative cooling. For cirrus cloud formation, the lifting mechanism often takes place on a synoptic scale on top of a frontal boundary, or at smaller scales due to turbulence close to a jet stream (Heymsfield et al., 2017). Jet engine emissions from aircraft are another cause of the development of cirrus clouds. At first, these so-called contrails will begin to form as the emitted particles get activated into water droplets. Contrails can either be short-lived or long-lived, where they have to remain for at least 10 minutes to classify as long-lived contrails (Kärcher, 2018). If the contrails stay persistent, they can further develop into clouds, called contrail cirrus. The contrail cirrus develops as the aircraft plumes interact with vortices at the edges, and gets spread out over time. Radiative cooling that occurs in the upper troposphere on moist air is another cause of cirrus cloud formation (Heymsfield et al., 2017). Cirrus clouds can either form by direct deposition of water vapor to ice, or by freezing of liquid droplets. Cirrus clouds from the first formation mechanism are called in situ origin cirrus, and those from the second mechanism are called liquid origin cirrus. Their microphysical properties differ, where liquid origin cirrus has higher ice water content (IWC). Consequently, they are optically thicker (Krämer et al., 2016).

Other types of pure ice clouds include polar stratospheric clouds or nacreous, also referred to as "mother of pearls" clouds, and noctilucent clouds. Polar stratospheric clouds occur in the polar region at altitudes from 15 - 17 km, at

temperatures colder than 190 K ($\sim -83°$C). Noctilucent clouds are formed at mid and high latitudes during the summer months at an altitude of 83 km, and a temperature below 150 K ($\sim -123°$C) (Kokhanovsky and Tomasi, 2020).

After addressing the large-scale mechanism leading to cirrus cloud formation, the microphysical properties of cirrus clouds will be described in the following section.

2.1.2 Formation and growth of ice crystals

Formation of ice crystals

Ice crystals in the atmosphere are predominantly the hexagonal crystal form of standard ice or frozen water. The hexagonal structure is a pattern of six oxygen atoms arranged as a lattice, with a hydrogen atom between every oxygen atom. The pattern is repeated by further H_2O molecules connected via the hydrogen bonds. The structure is stable for atmospheric pressure and for temperatures at which cirrus clouds form (Liou and Yang, 2016).

Ice formation can occur from two different phase transitions; either by freezing of a liquid droplet or by deposition of water vapor to the solid phase directly. Homogeneous and heterogeneous nucleation are processes that initiate the two phase transitions (Rogers and Yau, 1989). The first process, homogeneous nucleation, is the formation of ice from within a pure liquid cloud drop. The activated droplet needs to be supercooled and to have an ice-like structure, serving as an ice nucleus. Freezing from homogeneous nucleation depends on the surface free energy of the crystal-to-liquid interface. By this, smaller droplets will spontaneously freeze for colder temperatures than larger ones (Rogers and Yau, 1989). The temperature has to be close to -40° for the drop to freeze via homogeneous nucleation (Sassen et al., 2008). Homogeneous freezing of deposition is also possible but requires extreme conditions of supersaturation with respect to ice. Before this supersaturation is reached, liquid droplets will nucleate homogeneously. Moreover, at these cold temperatures, there are already few liquid droplets left in a cloud which implies that heterogeneous nucleation is a dominating process (Heymsfield et al., 2017).

As the temperature drops below -15°C there are already an appreciable amount of ice crystals in a cloud. These ice crystals are formed by heterogeneous nucleation, which is the process where ice nucleation in a supercooled liquid droplet or in a supersaturated parcel is initiated by foreign particles (Liou and Yang, 2016). The intrusion of an ice-nucleating particle (INP) with a liquid droplet makes the water molecules more tightly bound, with an ice-like structure. Hence nucleation of ice from a droplet can occur at lower supersaturation and higher temperatures than for homogeneous nucleation. There are multiple ways ice can be formed by nucleation from liquid water, as illustrated in figure 2.2. In a cirrus cloud, the nucleation mechanisms that occur are pore condensation freezing (David et al., 2019), condensation, and immersion freezing (Heymsfield et al., 2017).

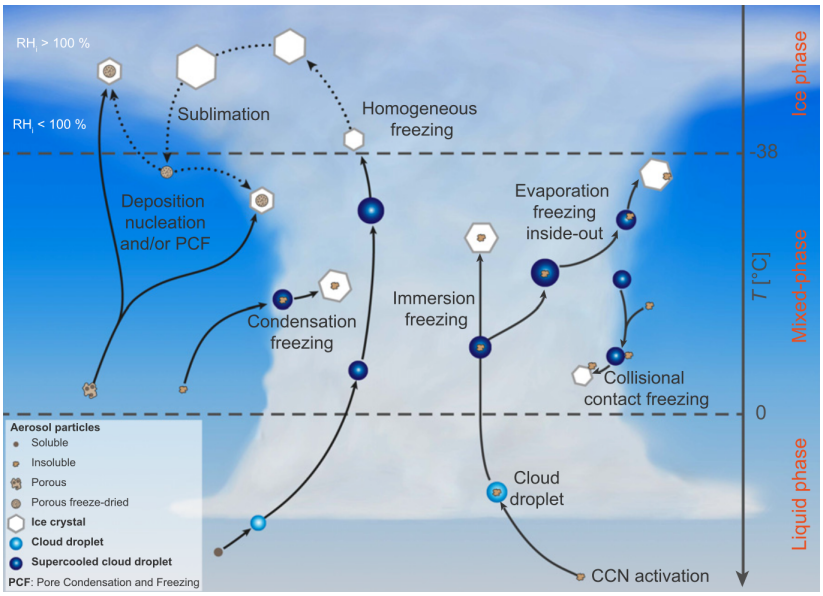

Figure 2.2: Different pathways of ice nucleation. Illustration from Kanji et al. (2017).

The concentration of ice crystals in a cirrus cloud is up to about 100 L^{-1} (Rogers and Yau, 1989). After the first ice crystals are produced by homogeneous or heterogeneous nucleation, secondary ice crystals will be produced. The mechanism for secondary ice production is the fragmentation of freezing drops, fragmentation due to ice-ice collision, and splintering of freezing drops (Korolev and Leisner, 2020). The first process occurs when liquid water is trapped inside

a freezing drop, and breaks the droplet when freezing. Fragmentation due to ice-ice collision is the process when smaller, weaker dendrites crystals collide with larger and denser graupel particles. The last process with splintering of freezing drops occurs when supercooled liquid droplets of the right size are captured by graupel particles, and small particles are ejected.

Growth of ice particles in clouds

After ice crystals are formed, they can further grow by deposition from water vapor. In an environment where supercooled droplets are dominant, the air is close to saturation with respect to liquid water and supersaturated with respect to ice. The ice particle will grow by deposition from water vapor much faster than the liquid droplet will grow from the vapor phase, as shown in figure 2.3. When the ice continues to grow, the vapor pressure will lower to the point below water saturation. Thus the ice particle can continue to grow (Wallace and Hobbs, 2006). This process is called the Wegener-Bergeron-Findeisen process.

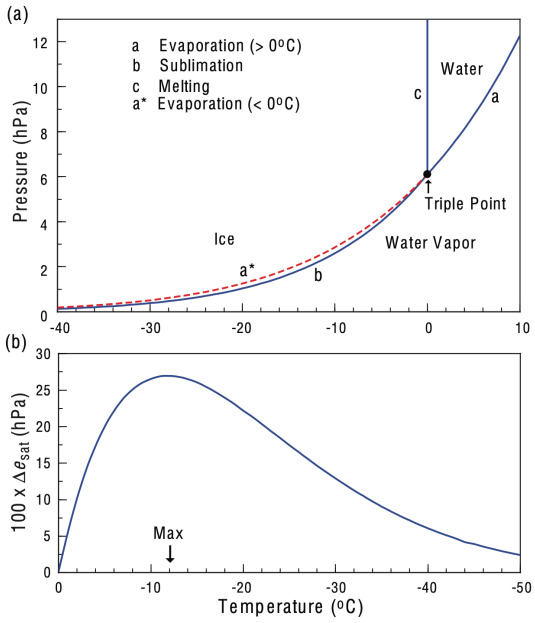

Figure 2.3: (a) Shows that saturation vapor pressure with respect to ice is lower than for liquid water. (b) Shows the difference in saturation vapor pressure between ice and water. Figure from Liou and Yang (2016).

The mass growth $\frac{dM}{dt}$ of an ice crystal by deposition from the vapor phase is defined as in (Liou and Yang, 2016):

$$\frac{dM}{dt} = 4\pi C D\,[\rho_v(\infty) - \rho_v(s)], \tag{2.1}$$

where C is the electrical capacitance of the ice crystal which depends on the shape and size of the non-spherical crystal, D is the molecular diffusion coefficient, $\rho_v(\infty)$ is the vapor density of the surrounding air, and $\rho_v(s)$ is the vapor density at the surface of the ice crystal. The parameter C can be set equal to r for a spherical crystal, or equal to $2r/\pi$ for a plate-type ice crystal with radius r. For ice needles, C can be approximated by the formula for a prolate spheroid (Liou and Yang, 2016). The mass growth equation (eq. 2.1) can be further derived by using 1) the Clausius-Clapeyron equation, describing the relation of temperature with saturation vapor pressure, and 2) the saturation ratio with respect to ice, S_i. The latter one can be set to:

$$S_i = \frac{e}{e_i}, \tag{2.2}$$

where e is the vapor pressure of the surrounding air, and e_i is saturation vapor pressure with respect to ice. The resulting growth rate can be described as follows:

$$\frac{dM}{dt} = \frac{4\pi C(S_i - 1)}{f_k + f_D}, \tag{2.3}$$

Where $f_k = L_I^2/(K R_v T^2)$ and $f_D = R_v T/[D\, e_i(T)]$.
L denotes the latent heat, K the thermal conductivity, R_v the specific gas constant for vapor, and $e_i(T)$ the vapor pressure with respect to ice for a temperature. The equations show that the growth of ice crystals by deposition from water vapor is a function of temperature and is inversely dependent on vapor pressure.

In a mixed-phased cloud ice particles can grow further with time by colliding with supercooled droplets. A second mechanism more common for cirrus clouds is growth by aggregation. This describes the processes of collision and coalescence. If ice particles have different fall speeds, they can collide with each other. The fall speed is determined by the shape and size of the ice particle. A cloud with

some rimed ice particles will have a larger collision frequency (Wallace and Hobbs, 2006). The second requirement of growth by aggregation is the ability of two ice particles to stick together after colliding. The coalescence efficiency is dependent on the ice particle shapes and the temperature. Consequently, ice crystal shape influences multiple microphysical processes, such as the growth of ice crystals in cirrus clouds. The main shapes of ice crystals include plates, columns, and dendrites with multiple variations within. The ice crystal shapes will be described in the next section.

2.1.3 Ice crystal habits

In contrast to liquid droplets, ice crystals have a non-spherical shape. The non-uniform deposition coefficient makes the growth rates of the crystal faces grow at different rates. The shape of an ice crystal is a hexagonal prism, with two primary habits; plate or column, as illustrated in figure 2.4. The two primary habits have different growth rates of their faces, resulting in different aspect ratios, c/a, where c is the thickness and a is the distance from the center face to one of the six corners (Lamb and Verlinde, 2011). The difference in evolution for the two primary habits is mainly dependent on temperature (Liou and Yang, 2016).

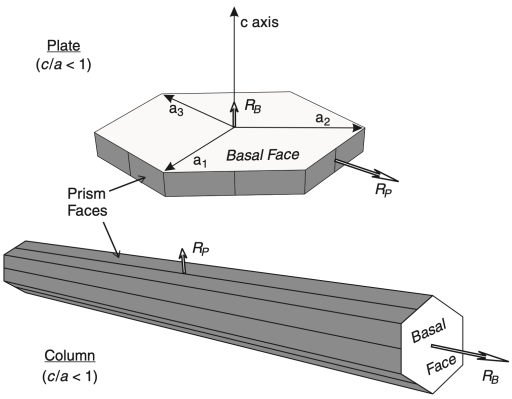

Figure 2.4: The two main primary ice crystal habits. Figure from Lamb and Verlinde (2011).

Further evolution of ice crystals can be categorized into secondary habits. Ice crystals can sublimate on the corner or the ends of the plate or column-like

ice crystal, respectively, depending on the saturation in the ambient air. For saturated air column-like crystals will develop as long and thin needles between -4 and -6° C. Under the same saturation conditions, plate-like crystals will develop into dendrites between temperatures from -12 to 16° C (Wallace and Hobbs, 2006). An overview of how the different ice crystal habits depend on the supersaturation and temperature is shown in figure 2.5.

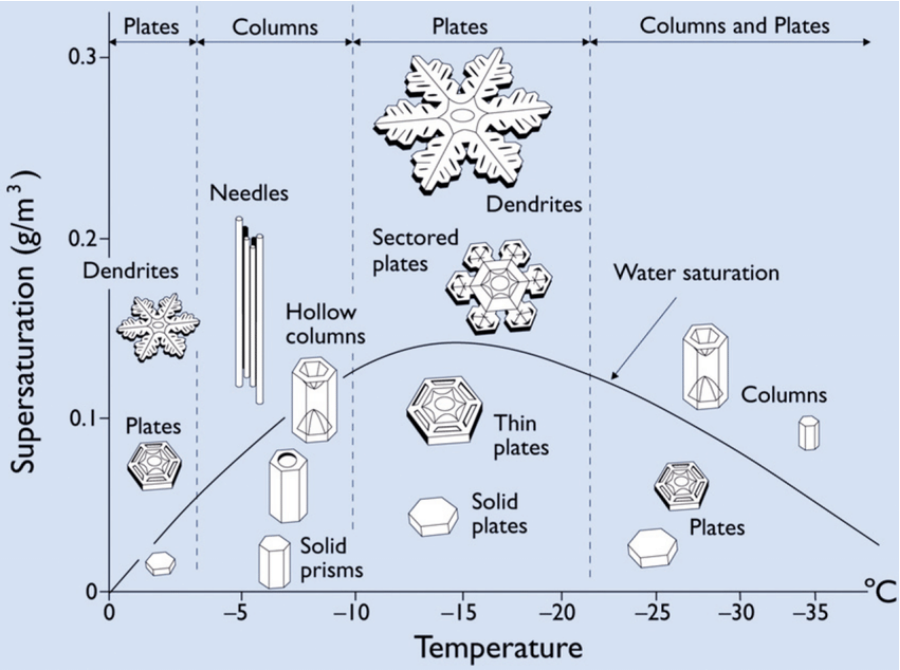

Figure 2.5: Different habits dependent on temperature and vapor supersaturation with respect to ice. Figure from Li (2021).

Ice crystal habits in cirrus clouds

The morphology of ice crystals in cirrus clouds varies over a broad spectrum. They can include both hollow and solid columns, plates, as well as bullets, and aggregates of columns and bullets (Baran, 2004). The asymmetrical shapes are the most common ones, also in Arctic cirrus clouds (Korolev et al., 1999). The ice crystals also vary in size from less than 10 μm to a few thousand micrometers. The smaller crystals occur at the cloud-top where the temperature is coldest, and larger crystals occur at higher temperatures further down in the cloud. The size of the crystals also depends on the type of cirrus, where cold cirrus has a typical crystal size of 24 μm, cirrus stratus of 42 μm, and warm cirrus of

49 μm (Liou and Yang, 2016). The huge variations in ice crystal size, shape, and orientation make them difficult to measure (Noel et al., 2006; Sassen et al., 2008).

2.2 Impact of cirrus clouds on the radiation budget

Arctic cirrus clouds have several impacts on climate, in addition to their radiative influence. These impacts include dehydration of the upper troposphere, modifying ozone through chemistry, and altering existing patterns of trace gases and INPs, where the latter again affects the properties of lower mixed-phased clouds (Schäfer et al., 2022; Kärcher, 2005). Their radiative impact on global climate will be further described in the next paragraphs.

Cirrus clouds have a strong impact on solar radiation (0.1 μm$-$3.5 μm), in the visible spectrum (0.4 μm$-$0.7 μm), and on terrestrial radiation that includes the infrared spectrum (3.5 μm$-$100 μm) (Thomas and Stamnes, 1999). This radiative impact affects the surface temperature (Wang, 2013). Cirrus clouds reflect a part of the incoming solar radiation back to space relying on the position, optical thickness, and ice crystal shape and size. The reflection leads to a cooling effect at the surface and at the top of the atmosphere (Heymsfield et al., 2017). Moreover, cirrus clouds will also absorb infrared radiation emitted from the surface. This radiation will be absorbed and re-emitted at a much lower temperature. Following from Stefan-Boltzmann's law which relates the irradiance emitted from a black body to its temperature to the power of 4, cirrus clouds would therefore trap terrestrial radiation and lead to a warming effect in the terrestrial wavelength range. The impact of cirrus clouds on incoming solar radiation, and terrestrial radiation is illustrated in figure 2.6. To give a measurement of the absorption, scattering, and emission of radiation propagating through the atmosphere, the equation of radiative transfer will be used (Chandrasekhar, 1960).

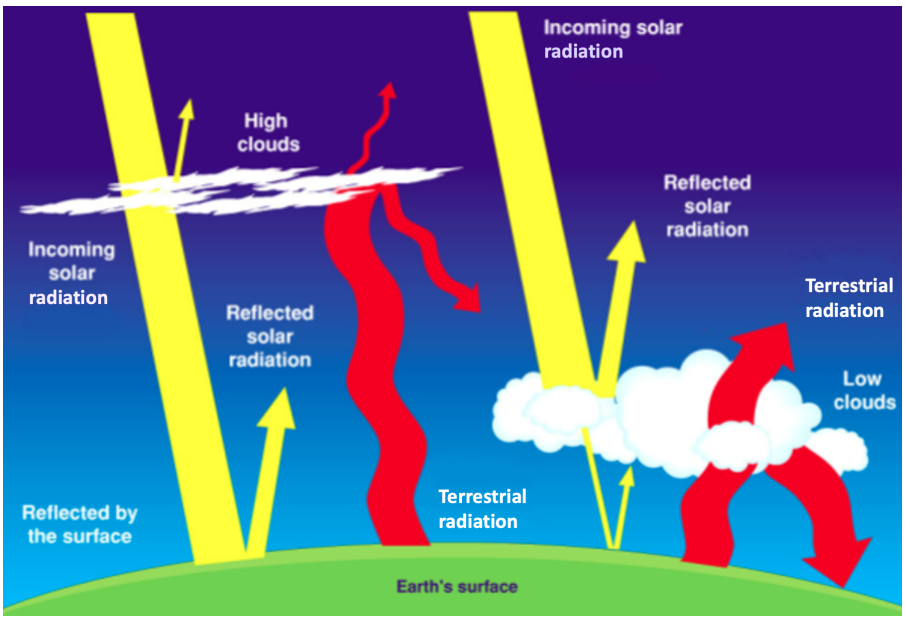

Figure 2.6: Impact of clouds on the radiation budget, where cirrus clouds fall under the category of "High clouds". Edited figure from NASA (2022).

2.2.1 Radiative transfer equation

As radiation propagates through the atmosphere and interacts with a cirrus cloud and other atmospheric constituents, the incident radiation is reduced due to absorption and scattering and increased due to the emission of volume elements along the propagation direction. These processes can be described with the radiative transfer equation (RTE; Chandrasekhar, 1960). The radiative transfer equation in plane-parallel geometry can be expressed as (Chandrasekhar, 1960):

$$\mu \frac{d}{d\tau} L(\tau, \mu, \phi) = L(\tau, \mu, \phi) - \frac{\omega_0}{4\pi} \int_0^{2\pi} \int_{-1}^{1} \mathcal{P}(\cos(\Theta)) L(\tau, \mu', \phi')\, d\mu'\, d\phi' - (1-\omega_0) B_{\text{Planck}}(T). \tag{2.4}$$

The variables are explained in table 2.1.

The first term represents the reduction of radiation due to extinction (scattering and absorption) along the direction of propagation. The second term describes the scattering of radiation from the incident direction (θ', ϕ') into the new direction (θ, ϕ) as characterized by the scattering phase function $\mathcal{P}$. Figure 2.7

Variables:	Description:
$L(\tau, \mu, \phi)$	The spectral radiance, dependent on the optical thickness τ, the zenith angle θ (since $\mu = \cos(\theta)$), and the azimuth angle ϕ of incoming radiation.
ω_0	Single-scattering albedo. This is the ratio of scattering efficiency and total extinction efficiency.
$\mathcal{P}$	The scattering phase function.
$\cos(\Theta)$	Cosine of the scattering angle Θ
$B_{\text{Planck}}(T)$	Planck's radiation law.

Table 2.1: Variables explained for the radiative transfer equation.

illustrates the change of direction Θ for a electromagnetic ray due to scattering at a non-spherical particle. The last term represents the enhancement of radiation due to thermal emission along the path of propagation.

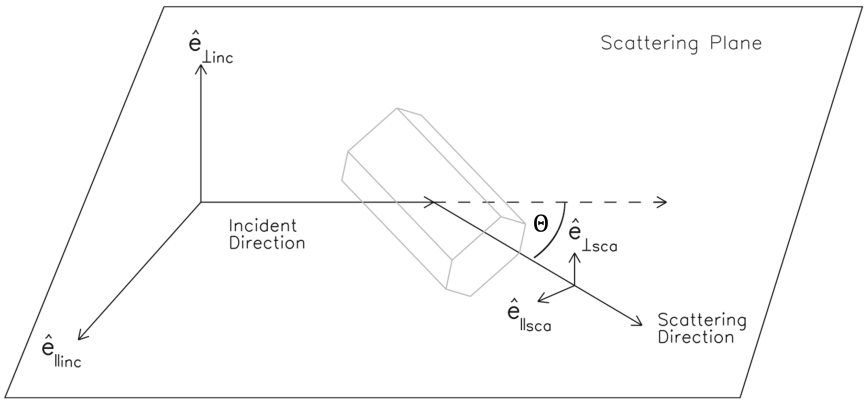

Figure 2.7: Geometry of the scattering of a plane electromagnetic wave at a non-spherical particle. The electro-magnetic field vectors are shown as $\hat{\mathbf{e}}$. Modified figure from Wendisch and Yang (2012).

In this study, we focus on the visible wavelength range, where the single-scattering albedo ω_0 is close to 1. Consequently, the thermal emission term can be neglected (Forster, 2017).

2.2.2 Ice crystal scattering phase function

To provide information on the optical properties of ice crystals, different solution equations can be used depending on the characteristics of the ice crystals. For

ice crystal sizes much larger than the wavelength of the radiation, the geometric optics approach can be used to calculate their optical properties (Liou and Yang, 2016). The scattering at the ice crystals is predominantly in the forward scattering direction and can be described by the phase function. The phase function for non-spherical ice crystals of the same size, but randomly oriented can be calculated as in Liou and Yang (2016):

$$\mathcal{P}(\Theta) = \frac{1}{2\pi\sigma_s} \int_0^{2\pi} \int_0^{\pi/2} \mathcal{P}'(\alpha', \gamma')\, \sigma_s'(\alpha', \gamma') \sin(\alpha')\, d\alpha'\, d\gamma'. \tag{2.5}$$

α' and γ' denote the orientation angles of an ice crystal dependent on the direction of the incident light beam, σ_s is the scattering cross section of non-spherical ice crystals, $\mathcal{P}'$, and σ_s' are the scattering phase function and the scattering cross section for a single ice crystal, respectively.

In the case of randomly oriented ice crystals, the phase function only depends on the scattering angle Θ. As an illustration, Forster (2017) show three scattering phase functions for ensembles of solid ice crystal columns with different effective radius r_{eff} as shown in figure 2.8. The plot shows two clearly forward scattering directions at angles 22° and 46°. In addition, the plot also shows that for larger ice crystals, with larger effective radius, the peaks of the phase function at 22° and 46° are more defined. These scattering angles produce halo displays, which makes the geometric optics approach suitable for explaining the halo display phenomena.

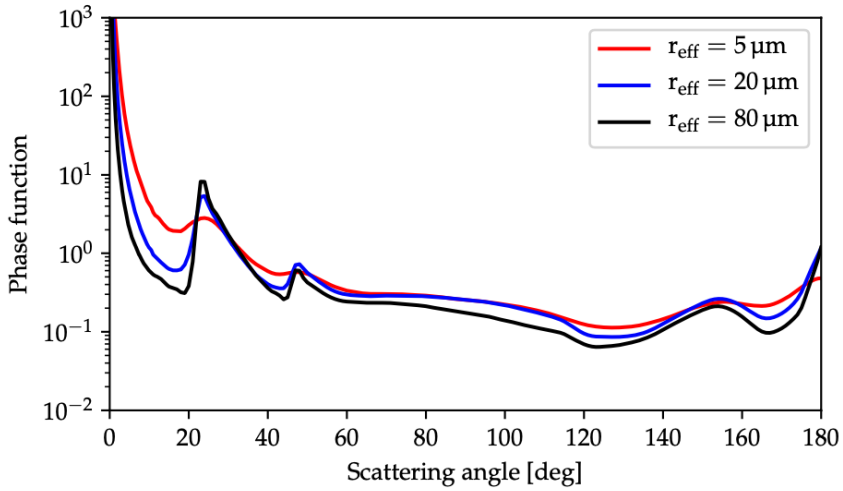

Figure 2.8: Scattering phase functions for smooth solid ice crystal columns at a wavelength of 550 nm, for three different effective radii r_{eff}. Plot from Forster (2017).

2.3 Halo displays

2.3.1 Different types of halo displays

Cirrus clouds are thin and their small optical depth makes it possible for solar radiation to shine through. This allows for fascinating optical phenomena called halo displays to arise. Halos are produced by the refraction and reflection of solar and moonlight by ice crystals (Wang, 2013, Zinkova, 2018). The halo displays can have different appearances in the sky depending on the orientation, shape, and size of the ice crystals. Figure 2.9 shows some of the different displays. The most common halo is the 22° halo which can be recognized as a circle of colorful light, going from red on the inside to blue on the edge, centered around the sun. Another type of circular halos is the 46° halo, appearing similar to the 22°, but placed further away from the sun. These circular halos are produced by randomly oriented ice crystals (Gedzelman, 2003). Other types of halos are the upper and lower tangent arcs, the Parry arc, and sundogs. These are produced by oriented columns and plates, which also makes them brighter as the oriented crystals will focus the light (Gedzelman, 2003). The ice crystals in the cirrus cloud has to be somewhat uniformly distributed for halo displays to be visible (Forster, 2017). As a 22° halo will be analyzed in section 4, in the

following we focus on the formation of circular halos using the geometric optics approach.

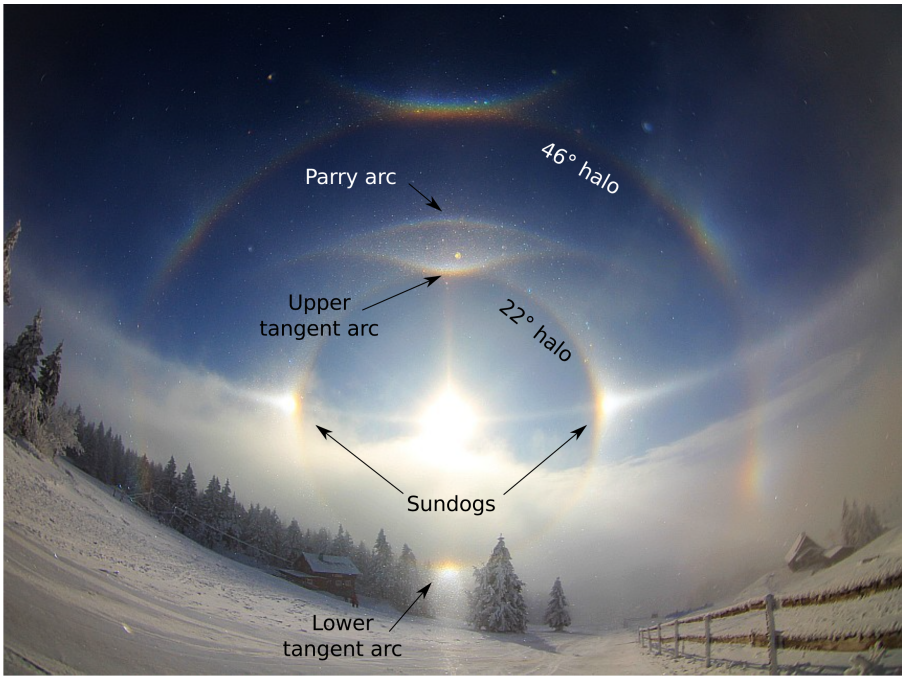

Figure 2.9: Different types of halo displays in ice fog photographed by Wolfgang Hinz in Neklid, Czech Republic. Edited by Linda Forster (Forster, 2017).

2.3.2 Formation of the 22° and 46° halos

The 22° and 46° halo is produced by refraction of light by randomly orientated hexagonal plates and columns. The principle is illustrated in figure 2.10 taken from Forster (2017), and in figure 2.11 from a person's perspective.

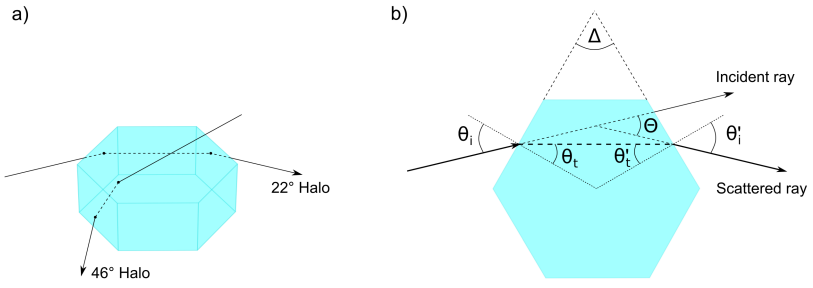

Figure 2.10: a) Hexagonal prism with 22° and 46° scattering angle. b) Notation of angles: θ_i is the incident angle, θ_t is the angle of refraction, Θ is the scattering angle of an ice crystal with prism angle Δ. Illustration from Forster (2017).

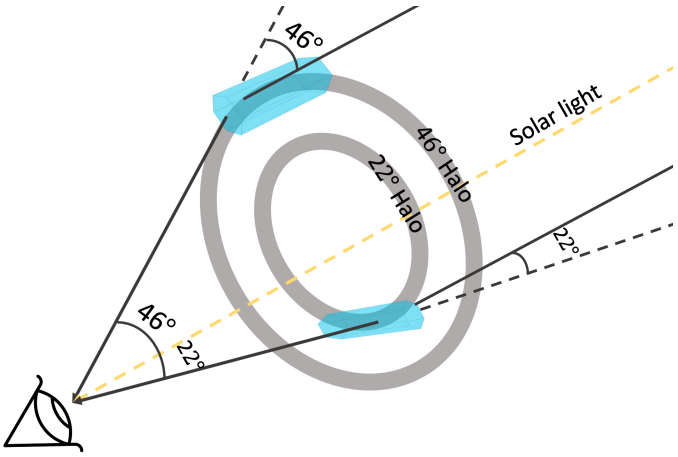

Figure 2.11: A persons perspective of the 22° and 46° halos from ground.

The difference between the two halo displays depends on the crystal faces the light is refracted at. For the 22° halo, the halo is produced when the light is refracted between two of the rectangular faces, which have an angle of 60° relative to each other. The 46° halo forms when the light is refracted between a rectangular face and a hexagonal face (Gedzelman, 2003). For a light beam passing through a hexagonal plate or column with angle Δ, the scattering angle Θ can be expressed as:

$$\Theta = (\theta_i - \theta_t) + (\theta_i' - \theta_t') = 2\theta_i' - \Delta, \tag{2.6}$$

where the different angles are shown and described in figure 2.10. The maximum intensity follows when the scattering angle is at its minimum Θ_{min} such that:

$$\frac{d\Theta}{d\theta_i} = 0. \tag{2.7}$$

Derivation of equation 2.6 with respect to θ_i at minimum yields:

$$\frac{d\Theta}{d\theta_i} = \frac{d\big((\theta_i - \theta_t) + (\theta_i' - \theta_t')\big)}{d\theta_i} = 1 + \frac{d\theta_i'}{d\theta_i} = 0. \tag{2.8}$$

When the scattering angle is at a minimum, the incident angle θ_i and the refraction angle θ_t can be expressed as:
$\theta_i = (\Theta_{min} + \Delta)/2$ and $\theta_t = \Delta/2$ respectively.

Furthermore, the incident and refraction angles are related to each other via Snell's law:

$$\sin(\theta_i)/\sin(\theta_t) = n, \tag{2.9}$$

where n is the refractive index of ice and assumes a refractive index of air of 1. Substituting the incident angle θ_i and the refraction angle θ_t with the minimum scattering angle Θ_{min} into Snell's law, we get:

$$n = \frac{\sin\left(\frac{\Theta_{min}+\Delta}{2}\right)}{\sin(\frac{\Delta}{2})}. \tag{2.10}$$

Hence, the minimum scattering angle Θ_{min} can be calculated for a known refractive index n and prism angle Δ. This equation can also explain the color pattern of halos. For longer wavelengths (red in color), the refractive index of ice is smaller than for shorter wavelengths (blue in color) (Forster, 2017). From Warren and Brandt (2008), the refraction index of ice can be set to $n = 1.3194$ for wavelengths of 400 nm (blue), and $n = 1.3049$ for wavelengths of 800 nm (red). From equation 2.10, the minimum scattering angle Θ_{min} for a 60° prism is calculated to be 22.55° and 21.45°, for the blue and red wavelengths respectively. The minimum scattering angle will thus be smaller with a smaller refractive index. This results in a halo with red color from the inner edge going towards blue for the outer edge.

Information on ice crystal properties from halo displays

As mentioned, the type of halo display is linked to the orientation of the ice crystals. Beyond the orientation, the scattering phase functions contain further information on ice crystal shape and size. Information on the shape of ice crystals can be retrieved from halo ratio (HR). This ratio is defined as the ratio of radiance measured at the greatest and smallest scattering angle (Auriol et al., 2001). For a circular halo to be visible the HR must be > 1. The halo ratio increases from hexagonal plates to columns with a stronger brightness contrast (Forster, 2017). At last, the size of the ice crystals is connected to the width of

the scattering halo peak. For larger ice crystals the peak is narrower, implying a more visible halo (Forster, 2017).

CHAPTER 3

Characterization and calibration of the HaloCam

3.1 Description of the HaloCam

A digital camera, Sony RXOII (DSC-RXOM2), was used to collect calibrated radiance images to gain information about present halos. The camera features an Exmor RS CMOS sensor, which means that the photodiodes are placed in front of the wiring, in contrast to a front-illuminated structure, as figure 3.1 shows. This makes the resolution higher for smaller sensors without decreasing light sensitivity (SONY, 2021). The CMOS image sensor has a size of 13.2 mm $\times$ 8.8 mm, with a number of 4832 $\times$ 3224 pixels. The lens has a horizontal and vertical field of view of 79.75° and 58.23° respectively, with an angular resolution of 0.1°. Further specifications of the camera are summarised in table 3.1.

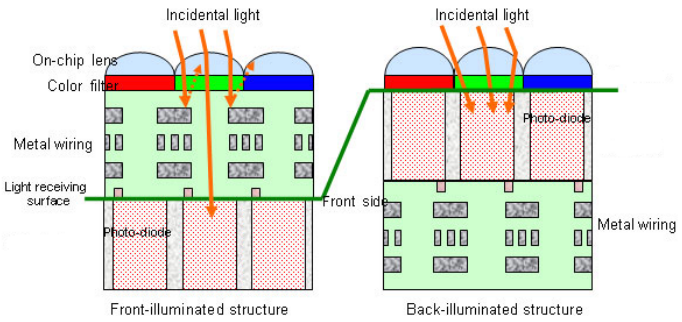

Figure 3.1: Difference between Front-illuminated (left) and Back-illuminated (right) structure. The HaloCam features a Back-illuminated design. (SONY, 2021).

Camera	Type	Sony RXOII (DSC-RXOM2)
	Dimensions	59.0×40.5×35.0 mm (W×H×D)
	Weight	132 g
Lens	Type	ZEISS Tessar T* Lens
	Apeture	F4.0
	Focal length	f=7.9 mm
	Horizontal field of view	79.75° (calculated)
	Vertical field of view	58.23° (calculated)
Sensor	Type	Exmor RS CMOS sensor
	Size	13.2 mm × 8.8 mm
	Number of pixels	4832 × 3224 (W× H)

Table 3.1: Specifications of HaloCam.

The sensor uses RGB color space, which consists mainly of three color components: red, green, and blue (Selek, 2016). For spectral response measurements, the color information is arranged on top of the sensor as a color filter array (CFA). The resulting pattern is a Bayer filter pattern as shown in figure 3.2. Each pixel represents a color channel, and the array can be divided into 2 × 2 pixel blocks which contain one red, two green, and one blue color value. To obtain altogether one red, green, and blue value for each pixel, a demosaicing algorithm was applied.

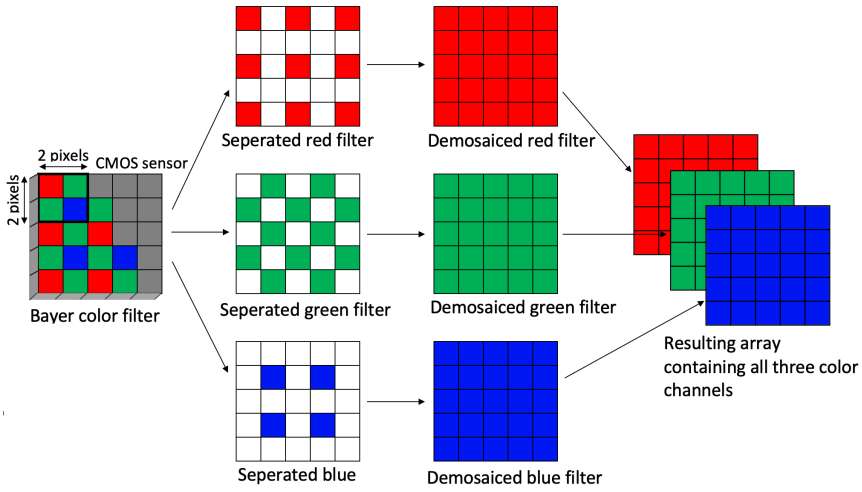

Figure 3.2: Process showing demosaicing of the Bayer CFA.

To analyze the halo displays captured on the images, the position of each pixel on the CMOS sensor must be transformed into spherical coordinates. This can be done by geometric calibration of the specific camera. In addition, to relate the measured pixel intensity to a physical quantity of radiance, with unit W m^{-2} nm^{-1} sr^{-1}, a radiometric calibration was executed. This makes use of the possibility to record raw images with the camera, enabling us to fully control the post-processing steps. To apply the radiometric calibration, the camera needs to be characterized to correct for camera defects, due to manufacturing differences, vignetting effect, etc. The characteristics include calculations of the linearity, dark current, electronic noise, and relative spectral response of the camera. The step-by-step characterization and subsequent radiometric and geometric calibration are further described in the next sections. Besides the post-processing of the raw camera images, all image analysis within this thesis is performed with the programming language Python.

3.2 Characterization of the camera

3.2.1 Post-processing of raw camera images

All calculations used the debayered CFA for each image. The post-processing of the raw camera images was performed using the open software tool DCRAW (Coffin, 2023). This photo decoder allows for the computation of the debayered array containing the red, green, and blue color channels as shown in fig 3.2. All pictures were taken with Sony's raw file format, ARW. The raw format ensures the recording of the uncompressed and unprocessed signal (Adobe, 2023). The debayered image was stored in the Tag Image File Format (tiff) file with the command:

```
dcraw -c -v -o 0 -t 0 -r 1 1 1 1 -T -4 image.ARW > image.tiff
```

To avoid any white balance to be applied to the image, the multipliers for all channels are set to 1 with the option "-r 1 1 1 1". The tiff image file is stored as 16-bit, to get the most possible information out of the image, by the option "-4". Hence the dynamic range of each pixel varies from 0 digital numbers (DN, dark) to 65536 DN (saturated). With all the image files stored as tiff files, the

debayered images can easily be read in with python for further processing.

3.2.2 Dark current

When no light is entering the camera lens, the image should appear completely dark, with a signal equal to zero. However, when taking a picture incident photons is converted into electrical energy by the photodiodes in the sensor (Keim, 2020). This cause a build-up of electrons on the sensor (Teledyne Photometrics, 2023). The build-up causes a small signal to appear, called dark current, which needs to be corrected. Dark current is dependent on temperature and exposure time (Carlsen, 2018). Two different exposure times at 1/1000 s and 1/320 s representative for field measurements have been used for the calculations. The dark current was calculated by taking the mean signal of 100 dark pictures. The probability densities for the dark current are shown in figure 3.3. For exposure times 1/1000 s, and 1/320 s, the dark current was calculated to be 6.14 DN and 6.02 DN, with a standard deviation of 0.22 DN and 0.24 DN, respectively. Keeping in mind that the highest possible signal is 65536 DN, the dark current is negligible.

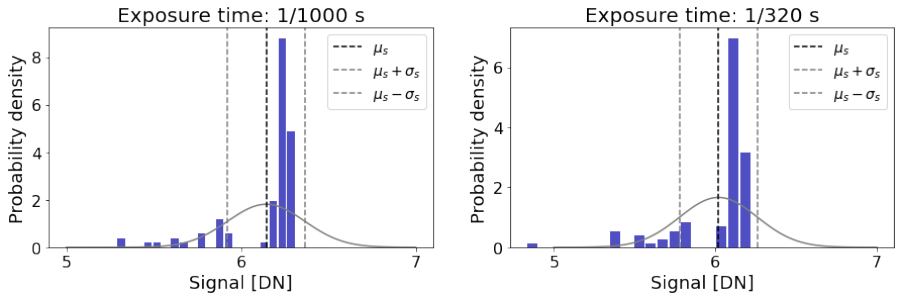

Figure 3.3: Probability densities for dark current plotted as histograms, with the associated normal distribution. Plotted for both exposure times, 1/1000s and 1/320 s, respectively. The vertical lines denote the mean μ_s signal and standard deviation σ_s.

As the dark current for exposure time 1/320 s doesn't vary much from exposure time 1/1000 s as figure 3.4 shows, the dark current seems to be independent of exposure time. For a more thorough analysis, more exposure times would need to be tested. However, also Forster (2017) showed that the dark signal is independent of the exposure time over a wide range of exposure times less than 50 ms. This is likely due to the fact that shorter exposure times will have

a lower read-out noise. This is the most common source of noise in a CMOS image sensor and is caused by the electrons getting exposed from analog to digital conversion (Oxford Instruments, 2023). A lower read-out noise is wanted because the sensor will detect low-level signals more easily, and achieve a high dynamic range (Oxford Instruments, 2023). To correct for the dark current of the camera, the mean value of the dark current calculated for the two exposure times was used for each channel. The values are shown in figure 3.4 expressed as 6.59 DN (red), 5.16 DN (green), and 6.50 DN (blue).

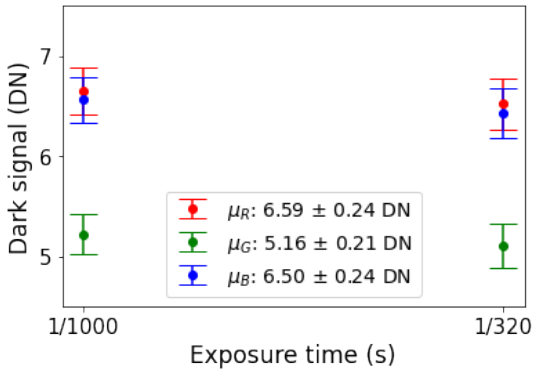

Figure 3.4: Dark current and dark current noise for red, green, and blue color channels. Shown for two exposure times representative for field measurements. The calculated average and standard deviation for 100 dark photos over both exposure times are denoted as μ_R, μ_G, and μ_B for the red, green, and blue color channels, respectively.

3.2.3 Linearity

To use the camera for analyzing the halo displays, the intensity of radiance going into the sensor and the final signal generated by the sensor should show a linear relationship. This allows for the application of the radiometric calibration (see Sect. 3.3) over a wide range of natural illumination conditions. The linearity of the CMOS sensor was characterized similarly to Carlsen (2018) where pictures were taken of a stable, diffuse light source (integrating sphere). Figure 3.5 b) shows the integrating sphere with the HaloCam placed in front. A light source from a 100 W frosted lamp enters the coated sphere where the radiation gets reflected multiple times before leaving the sphere through the aperture, as illustrated in figure 3.5 a). The outgoing radiation is completely uniform

and diffuse and, thus, suitable for the linearity measurements and subsequent calibration steps.

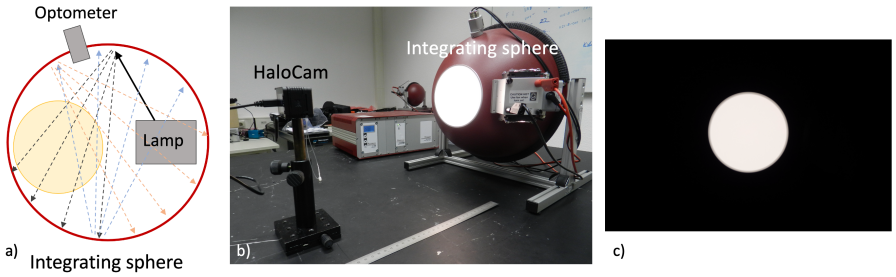

Figure 3.5: (a) Illustration of integrating sphere as diffuse and uniform radiation source. (b) The setup of the integrating sphere with the HaloCam in front. (c) Resulting HaloCam example picture for the center of the sensor.

The pictures were taken for different exposure times, ISO numbers, and for different intensities of the light source. For all variables, the f-number was set to f/4. The exposure time measurements had a constant ISO number set to 80. Pictures were then taken for 40 different exposure times varying from 1/32000 s to 1/4 s. The relation between the ISO number and the signal was measured with constant exposure time at 1/5000 s, for 23 different ISO numbers from 80 to 12800. Finally, the intensity of the integrating sphere was measured with the optometer current decreasing from the maximum at $0.7438\,\mu A$ to zero, with ISO and exposure time set to 125 and 1/200 s, respectively. The linear relations were calculated by taking the average signal for the illuminated spot for each image. Figure 3.6 shows the linearities for the signal generated by the sensor dependent on exposure time, ISO number, and intensity. As illustrated in the figure, the relation between the signal and the incident radiation is linear. The measurements were executed both for the center of the sensor and for the edge to check for non-uniformities across the sensor. As figure 3.6 shows, the slope is steeper for the center of the sensor. This can be explained by the vignetting effect, which will be characterized in section 3.3. Where the linear pattern turns into constant points for increasing incident radiation, the picture is overexposed and the signal saturated.

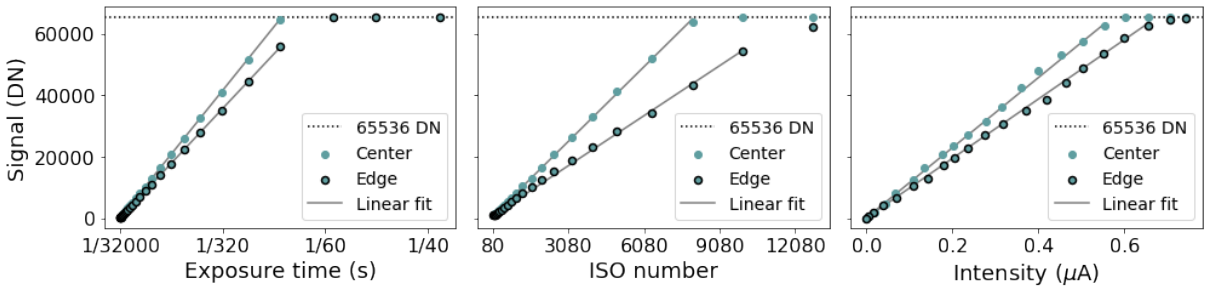

Figure 3.6: The linearity of the signal is dependent on exposure time, ISO, and intensity from left to right for the red color channel.

The root mean square error (RMSE) for the linear fit is shown in table 3.2. Since the RMSE values are relatively small compared to the dynamic range of the measured signal, the linearities are validated. Hence, the camera is suitable for halo display measurements.

	Center	Edge
Exposure time (DN)	99	108
ISO number (DN)	535	129
Intensity (DN)	412	138

Table 3.2: Root mean square error (RMSE) for linear regression calculated for Exposure time, ISO number, and Intensity.

3.2.4 Relative spectral response

Characterization of the spectral response for the HaloCam color filters is essential for the radiometric calibration in section 3.3. The spectral response defines the photodiodes sensitivity to different wavelengths of radiation, which includes the visible spectrum (Rensselaer Polytechnic Institute, 2004).

The relative spectral response (RSR) was measured using a monochromator (type Omni-lambda 3005 Zolix) in front of the sphere, as shown in 3.7 (a). The radiation leaving the aperture from the integrating sphere enters the monochromator, where it interacts with mirrors and a tiltable grating. The tiltable grating scatters the radiation beam and separates the wavelengths. Depending on the angle of the tilt, the desired wavelengths of the radiation

associated with a color channel will leave the monochromator through a slit opening. The HaloCam is placed in front of the opening taking pictures of the slit. The RSR was calculated from the pictures in a similar way as described in Carlsen (2018), Forster (2017), and L. Forster et al. (2020). The RSR can be described as the function:

$$\mathrm{RSR}(\lambda) = \frac{T_c(\lambda)}{\int_0^\infty T_c(\lambda)\, d\lambda} \tag{3.1}$$

where the RSR carries the unit nm^{-1}, $T_c(\lambda)$ are the spectral transmission coefficients for each color channel c (red, green and blue). The wavelength λ of the radiation passing through the exit slit varies from 300 to 750 nm in 5 nm steps. For each picture, the average signal $s_c(\lambda)$ over the pixels covering the slit was calculated, with the dark current subtracted. The spectral transmission coefficients $T_c(\lambda)$ can than be calculated from the signal $s_c(\lambda)$ and the spectral radiance $I_{sphere}(\lambda)$ passing the aperture from the integrating sphere:

$$T_c(\lambda) = \frac{s_c(\lambda)}{I_{\mathrm{sphere}}(\lambda)} \tag{3.2}$$

Where s_c carries the unit DN, and I_{sphere} has the unit W m^{-2} sr^{-1} nm^{-1}.

The RSR function is normalized so that:

$$\int_0^\infty \mathrm{RSR}(\lambda) d\lambda = 1 \tag{3.3}$$

The normalized RSR sensitivity curves are shown in figure 3.7 (b) calculated by equations 3.1 to 3.3.

The characteristic of the RSR functions can be described by their central wavelength and their spectral bandwidth (Wang et al., 2020). The central wavelengths for the camera are 617 nm (red channel), 546 (green channel), and 477 (blue channel). The spectral bandwidth is calculated from the full width at half maximum and yields 66 nm (red channel), 124 nm (green channel), and 76 nm (blue channel). The characteristics are summarised in tabel3.3.

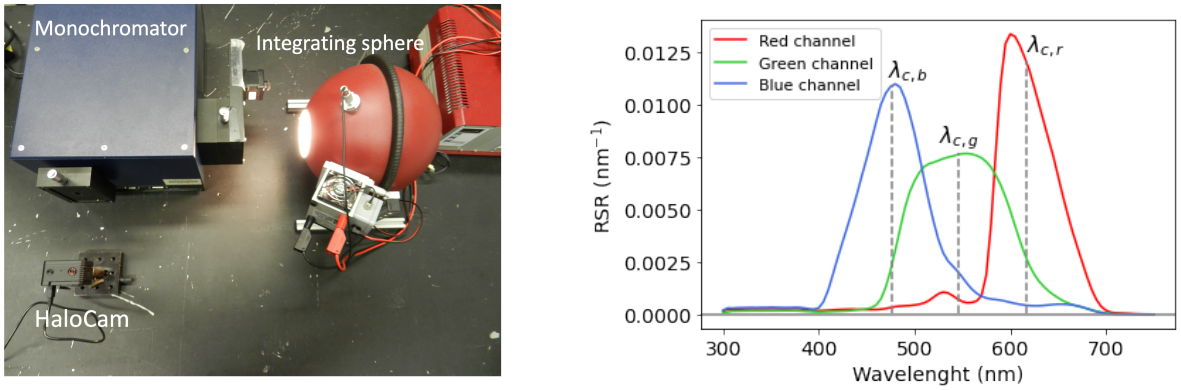

Figure 3.7: (a) Setup for spectral response measurements: integrating sphere with monochromator and HaloCam. (b) RSR function for the red, green, and blue color channels.

Color channel	Central wavelength λ_c (nm)	FWHM (nm)
Red	617	66
Green	546	124
Blue	477	76

Table 3.3: Central wavelengths λ_c and FWHM for each color channel of RSR functions.

3.3 Radiometric calibration

A radiometric calibration of the HaloCam is necessary to convert the measured signal in DN to a physical quantity for radiance that carries the unit W m^{-2} nm^{-1} sr^{-1}. In addition, each pixel on the sensor will have slightly different signals even for a uniform light source, due different responses of each photodetector. This noise pattern is called photo response non-uniformity (PRNU), and is temporally constant and unique for each image sensor (Dirik and Karakucuk, 2014). Moreover, the center of an image tends to be brighter than the edges. This is called the vignetting effect and is caused by imperfection of the aperture and by the spherical shape of the lens (Cao et al., 2020). For a perfect sensor, a picture of the integrating sphere opening, with uniform outgoing radiation, will result in an image with an equal signal for every pixel. Since this will not be the case, the PRNU and the vignetting effect needs to be corrected.

The measurements for the radiometric calibration was executed by placing the HaloCam in front of the integrating sphere. 100 pictures were taken while the camera was rotated. Thus, the illuminating integrating sphere opening covered every pixel of the camera sensor at least once. The resulting pictures have a bright circle (or half-cirlce) that is placed slightly differently for each picture, as shown in the collection of calibration pictures in figure 3.8.

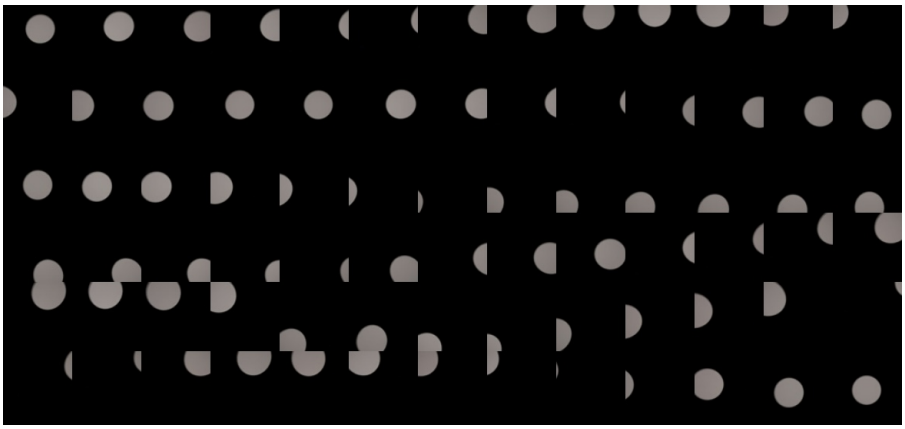

Figure 3.8: Collection of 70 example pictures of the illuminating integrating sphere opening before the pictures were stitched together.

The final, stitched image was then calculated by combining all the bright pixels from the 100 images. When a pixel was illuminated in more than one image, the average pixel signal was calculated to obtain the dynamic 16-bit range. Due to manufacturing differences and camera defects the stitched image had some pixel values deflecting from the overall signal pattern. Thus a Gaussian distribution was fitted to the image to make it completely smooth. As expected, the vignetting effect clearly emerges in the stitched image as shown in figure 3.9.

To apply the radiometric calibration, a calibration factor $k_c(x, y)$ is calculated for each pixel location (x,y) following Carlsen (2018):

$$k_c(x, y) = \frac{I_{\text{sphere}}(\lambda)}{s(x, y)} \cdot t_{\text{exp}}, \tag{3.4}$$

where $s(x, y)$ is the signal at each pixel in DN, t_{exp} is the exposure time used for the calibration (set to 1/500 s), and $I_{\text{sphere}}(\lambda)$ is the radiance emitted by the

integrating sphere in units W m^{-2} nm^{-1} sr^{-1}. The calibrated output of the integrating sphere itself is traceable to the National Institute of Standards and Technology (NIST) standards. This NIST-traceable output I_{ref} of the integrating sphere has been determined in the laboratory for a defined optometer current $\mathcal{I}_{\text{sphere}}$ of 0.5936 μA. Consequently, $I_{\text{sphere}}(\lambda)$ can be calculated by:

$$I_{\text{sphere}}(\lambda) = \frac{\mathcal{I}_{\mu}}{\mathcal{I}_{\text{sphere}}} \cdot I_{\text{ref,int}}(\lambda), \tag{3.5}$$

where $\mathcal{I}_{\mu}$ is the actual, average optometer current during the calibration (in μA). For this calibration, $\mathcal{I}_{\mu} = 0.4029\,\mu A$. The spectral radiance $I_{\text{ref,int}}(\lambda)$ that is measured by the CMOS sensor is defined as:

$$I_{\text{ref,int}}(\lambda) = \int_0^{\infty} I_{\text{ref}}(\lambda) \cdot \text{RSR}(\lambda)\, d\lambda, \tag{3.6}$$

which accounts for the relative spectral response RSR(λ) as defined in section 3.2.4. Combining equations 3.5 and 3.6, the final calibration factor is set to:

$$k_c(x,y) = \frac{I_{\text{sphere}}(\lambda)}{s(x,y)} \cdot t_{\text{exp}} = \frac{0.7 \cdot I_{\text{ref,int}}(\lambda)}{s(x,y)} \cdot t_{\text{exp}}. \tag{3.7}$$

The calibration factor $k_c(x,y)$ is shown in figure 3.9 for the red camera channel. The calibration factor is larger at the edges of the image than at the center and decreases by about 74% compared to the center. This can be explained by the fact that the edges tend to be darker with a lower signal due to the vignetting effect.

For comparison, a second calibration factor was calculated for different camera settings. For the second configuration, the ISO number, and f-number, were equal to the first configuration and set to 125, and f/4, respectively. However, the exposure time was set to 1/1000 s instead of 1/500 s as stated for the first configuration. Figure 3.10 (a) shows the calibration factor for the second configuration and (b) the ratio between the first and the second configuration. Figure 3.10 (a) shows that the vignetting effect is clearly present for configuration 2 as well, with a decrease of 67% from the edges towards the center. The

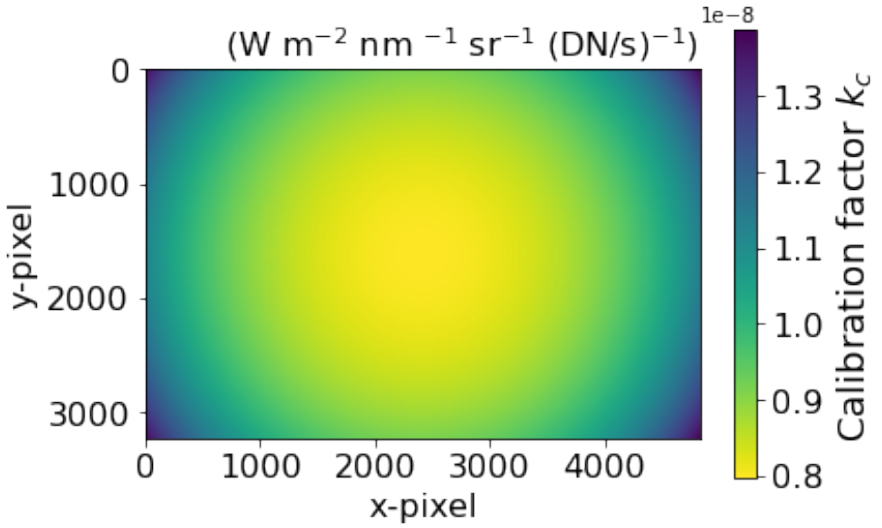

Figure 3.9: Calibration factor k_c for red camera channel, with ISO number set to 125, f-number set to f/4, and exposure time 1/500 s.

vignetting effect behavior is slightly different for the two exposure times, where the effect is larger for configuration 1.

For a longer exposure time, more radiation has time to enter the shutter. Hence, the image will be brighter for the first configuration with a higher calibration factor as figure 3.10 (b) shows. This figure also shows that the ratio between the configurations is larger at the edges of the sensor, confirming the difference in the present vignetting effects. This can entail that the total amount of radiation entering the system will also affect the degree of vignetting effect. However, the 22° halo will appear closer to the center where the ratio is more uniform as figure 3.10 (b) shows.

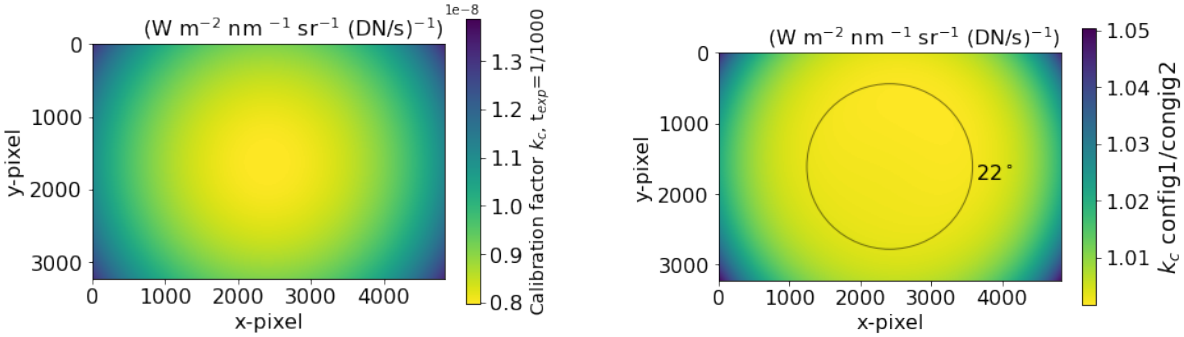

Figure 3.10: (a) Calibration factor for the second camera configuration (red color channel), ISO number set to 125, f-number set to f/4, and exposure time is set to 1/1000 s. (b) The ratio between the calibration factors of configuration 1 and configuration 2, with exposure time 1/500 s and 1/1000 s, respectively. The circle represents the position of a 22° halo.

3.4 Geometric calibration

To relate each pixel to a spherical coordinate, with an azimuth and a zenith angle, a geometric calibration is needed. Halo displays are optical single-scattering phenomena caused by ice crystals scattering light. Thus the scattering angle of a halo display relative to the sun can be directly linked to the camera viewing zenith angle (CVZA; Forster, 2017). For this thesis, the CVZA is calculated as a first-order approximation of the camera model, where lens distortion towards the edges is neglected. Assuming a pinhole camera model, the camera viewing zenith angle ϑ was calculated by:

$$\vartheta = \arctan \frac{d}{f}, \tag{3.8}$$

where d is the distance from a pixel coordinate (x, y) to the center of the image (x_0, y_0), which is dependent on the sensor size. The HaloCam has a sensor size of 13.2 mm × 8.8 mm. f is the camera's focal length of 7.9 mm. Figure 3.11 (a) shows the relationship between the pixel positions and the CVZA. For reference, a circle at a scattering angle of 22° is given that corresponds to a 22° halo assuming the sun is centered in the image. The camera viewing azimuth angle (CVAA) φ was calculated assuming a pinhole camera model as:

$$\varphi = \arctan \frac{d_x}{d_y}, \tag{3.9}$$

where d_x is the distance from the x-center point x_0, and d_y is the distance from the y-center point y_0. The CVAA is shown in figure 3.11 (b). As in Forster (2017) the CVAA is divided into 5 image segments, covering the upper part of the picture. The upper part of the picture usually contains the most valuable information of a 22°, as the lower part can be blocked by the horizon, especially under Arctic conditions with low Sun elevations. The first segment starts at CVAA of 105° and the last segment ends at CVAA of 255°, with 30° between each segment. Defining these segments is useful for later calculations of the scattering phase functions of the halo.

From the image size and the focal length, the horizontal and vertical field of view (FOV) can be calculated to be 79.75° × 58.23° (HFOV × VFOV).

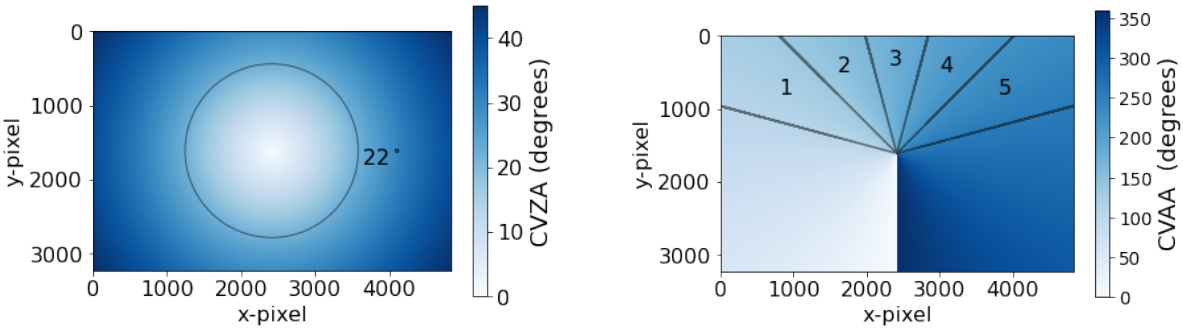

Figure 3.11: (a) Camera viewing zenith angel. The circle is marked at 22° scattering angle. (b) Camera viewing azimuth angel. The vertical lines divide the image into 5 segments, which will be used to calculate the radiance distribution of a halo photography, in section 4.2. The segments are ranging between 105°-255° with a step 30°.

CHAPTER 4

Arctic Halo case study

In this chapter, a case study of a halo display produced by an Arctic cirrus cloud is presented. An overview of the case study is described in section 4.1. Then, the methodology for retrieving the ice crystal properties is described in section 4.2, where the radiance distribution from the image is compared to simulations by a radiative transfer model. The third section 4.3 describes the resulting ice crystal properties in the cirrus cloud.

4.1 Arctic cirrus case on 22 February 2023

During February and March 2023, the University of Oslo lead the Mixed-phase Clouds and Climate (MC^2) campaign based at Andøya Space AS in Andenes, Norway. The overall objective of the campaign was to characterize the phase of cold clouds and study ice formation processes. The measurement efforts were focused around in-situ cloud observations conducted with the Beechcraft King Air C90 GTx research aircraft operated by the National Institute for Aerospace Research "Elie Carafoli" (INCAS) in Bucharest, Romania. The airborne observations were accompanied by a comprehensive suite of ground-based in situ and remote sensing instruments, which included the use of the HaloCam to characterize the ice crystal shape of Arctic cirrus clouds.

Andenes is located at 69° 18' 51.41" N and 16° 07' 9.80" E on the island of Andøya at the coast of Northern Norway as shown in figure 4.1. The area lies about 300 km north of the Arctic Circle (Evers, 2022). The location at the North Atlantic Ocean makes Andenes particularly exposed to Arctic weather conditions. The winter and spring can be characterized by snowy, cold weather

with frequent cloud cover. The spring in particular is often influenced by Cold Air Outbreak or Warm Air Intrusion conditions. A study conducted by Schäfer et al. (2022) found that 95% of the observed single-layer clouds with cloud base heights between 4,000 and 12,000 m and a cloud top temperature below 20°C over Andenes are pure ice clouds, such as cirrus clouds.

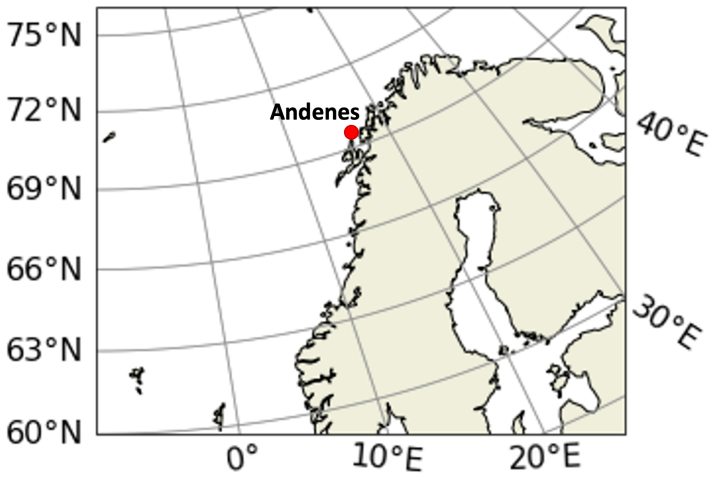

Figure 4.1: Andenes is marked with a red circle on the map. The village is located within the Norwegian Arctic at 69° 18' 51.41" N and 16° 07' 9.80" E.

On 22 February 2023, a cirrus cloud that produced a 22° halo was observed. An overview of the pressure systems for the time period is shown in figure 4.3. At 00:00 UTC on 22 February, a low pressure system was situated west of Trondheim outside the mid-coast of Norway. The pressure system was associated with a warm front, pointing towards the coast, with a following cold front. Figure 4.3 (b) shows that the system was moving quickly northward towards Andenes, and at 00:00 UTC on 23 February the fronts had already occluded and moved past Andenes. The warm front moving towards Andenes produced a cirrus cloud on top of the frontal boundary at daytime. The halo display was captured by the HaloCam at 11:50 UTC. Figure 4.2 shows the halo display together with cirrostratus clouds, which typically are produced in such frontal systems.

Figure 4.2: Halo display at Andenes, Norway, on 22 February 2023. Photographed by Tim Carlsen.

Figure 4.4 shows a two-hour forecast of (a) the fractional cloud cover for 11:00 UTC on 22 February right before the captured halo. This forecast materialized very precisely based on the local cloud observations at that time. The cloud cover was dominated by high clouds (overcast conditions), with no low clouds and only a small fraction of medium clouds (0.3) visible. These broken, mid-level clouds were only moving in from the west of Andenes and did not influence the observations at the time of the halo display. According to Figure 4.4 (b), the cloud base and top were approximately at around 7,000 m and 9,000 m, respectively. Hence, the cirrus cloud had a vertical extension of about 2,000 m. These cirrus cloud heights and vertical extensions are typical for Andenes in winter (Schäfer et al., 2022).

To obtain a coherent overview of the vertical atmospheric conditions, the temperature and Relative Humidity (RH) profiles from a radiosonde ascent at Andenes (launched at 11:00 UTC) are plotted in figure 4.5. The RH profile shows a strong increase in relative humidity at altitudes of 4,000-5,000 meters, indicating some medium-level clouds, which agrees with the forecast in figure 4.4 (a). The RH stays at about 80% (with respect to water). As the temperature between 4,000 m and 11,000 m altitude decreases, the RH with respect to ice increases from 110% (at -40°C) to 120% (at -50°C) and 129% (at -60°C,

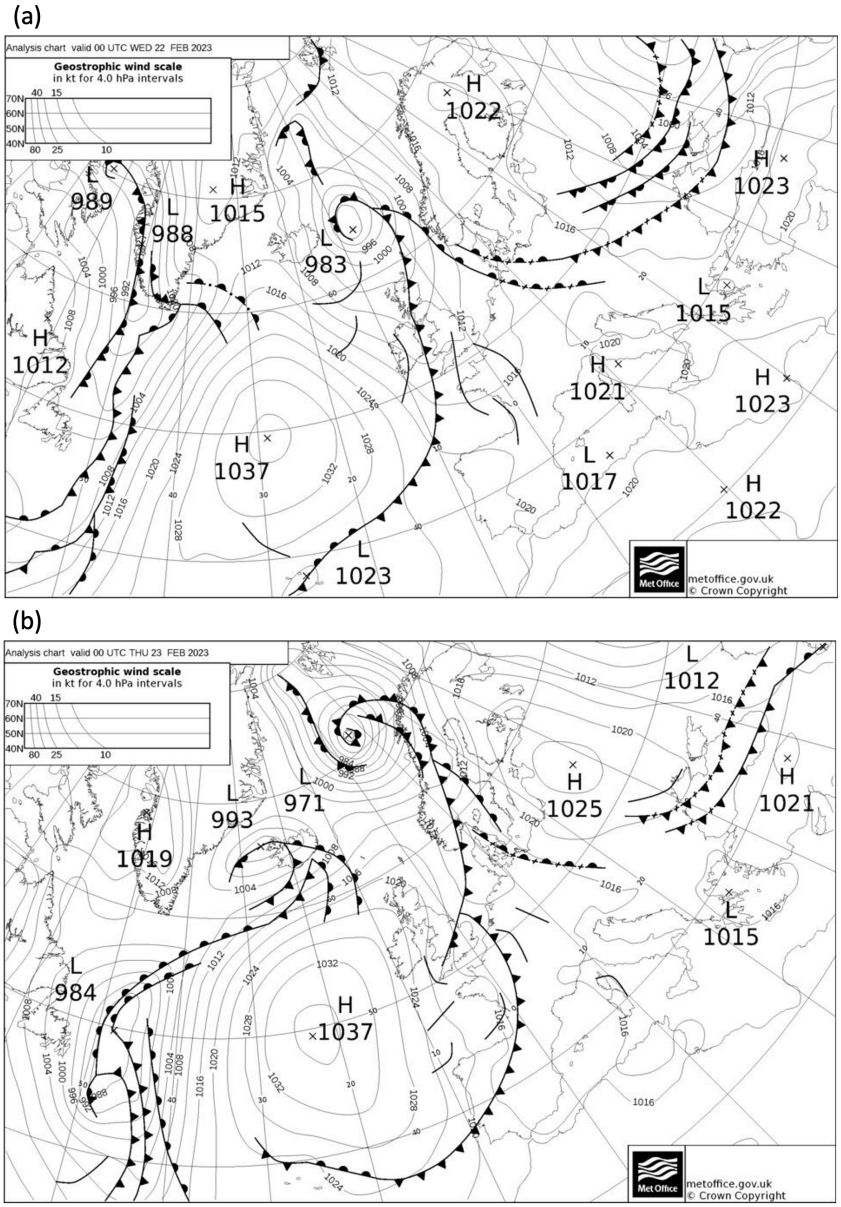

Figure 4.3: Surface pressure charts (from metoffice.gov.uk, 2023) show the surface pressure at 00:00 UTC for (a) 22.02.2023 and (b) 23.02.2023.

Murphy and Koop, 2005) providing supersaturated conditions in the cirrus regime. The vertical extension of the cirrus cloud appears a bit larger in the radiosonde profile than estimated above. However, as the radiosonde is drifting from the launch location with the wind, we estimated the cirrus cloud base and top from aircraft observations above Andenes (based on the presence of cloud

particles observed by the in situ cloud probes). Thus, the temperature at the cirrus layer is about -40 °C to -50 °C based on the temperature profile in figure 4.5 (a). The colder temperatures occur higher up in the cloud, where the ice crystals are also smaller. As the temperature is below -40 °C and the thus the homogeneous freezing level, the cloud is a pure ice cloud. The cirrus cloud will be further analysed by retrieving the information content from the 22° halo. The methodology for this retrieval is described in the next section.

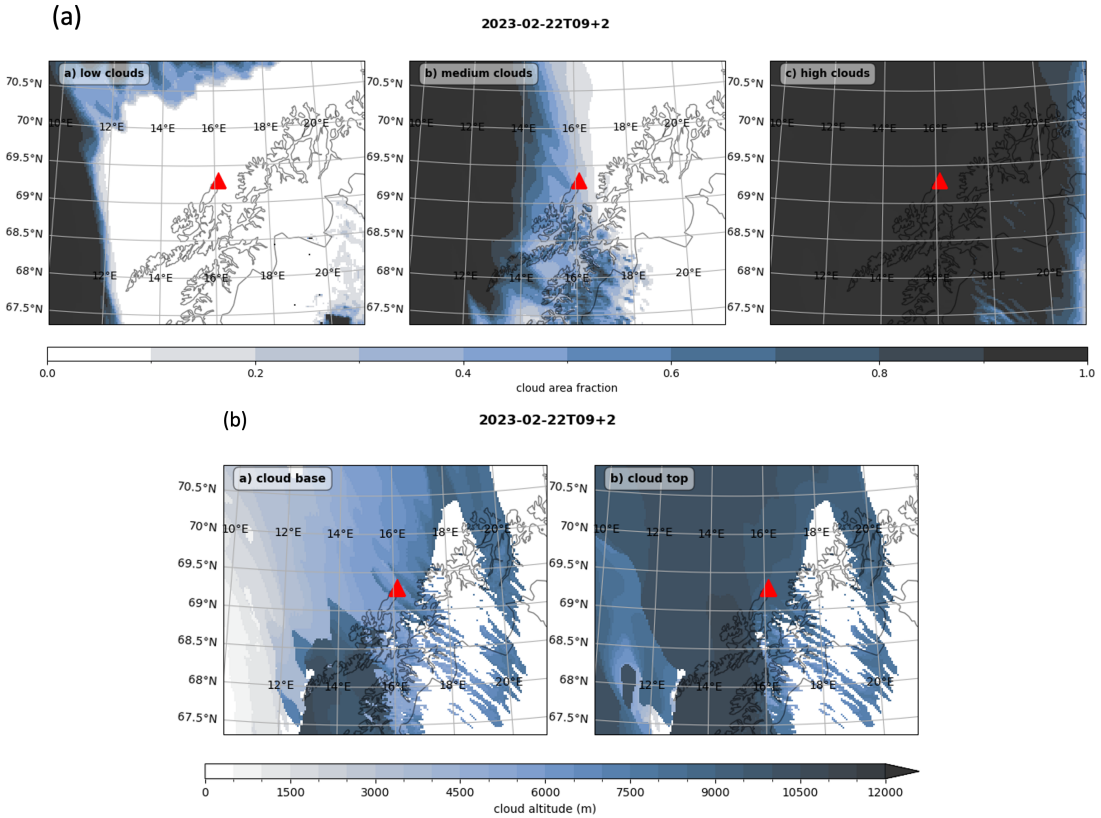

Figure 4.4: Two-hour forecast from 22.02.23 at 09:00 UTC of cloud layers over Andenes (marked with a red triangle) where (a) shows the fraction of a) low, b) medium, and c) high clouds, and (b) shows the a) cloud base and b) cloud top height. Forecast from Arome Arctic, data from MET Norway, figure courtesy of Franziska Hellmuth.

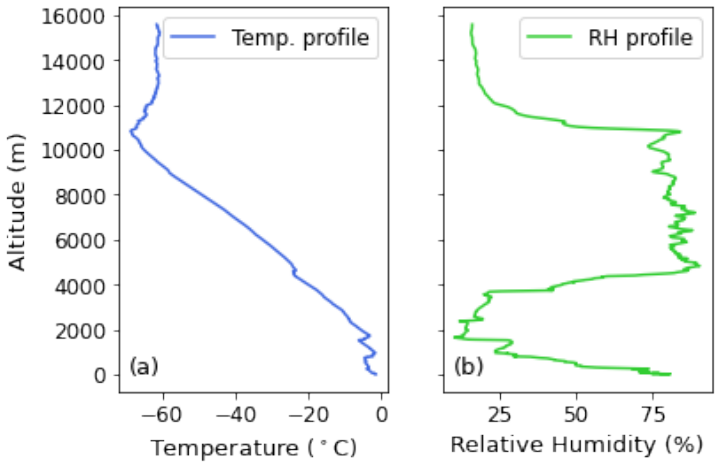

Figure 4.5: Data from radiosonde launched at Andenes on 22 February 2023 at 11:00 UTC showing atmospheric profiles of (a) Temperature in °C and (b) Relative Humidity (RH) in %. Data from MET Norway.

4.2 Methodology for retrieval of ice crystal properties

Post-processing of raw halo image

With a calibrated camera, the radiance distribution can be calculated from the raw halo image (see Fig. 4.2) using the radiometric calibration factor as defined in section 3.3 (eq. 3.7) and accounting for the camera configuration used during the measurement (exposure time, ISO value). For each image segment as defined in section 3.4, the radiance of the red camera channel was averaged over the scattering angle with a 0.1° resolution. The radiance distribution from segment 4, as shown in figure 4.6, was compared to forward simulations with a radiative transfer model to find the best fit. In principle, the radiance distribution can give information about the cirrus cloud optical thickness (COT), and the brightness contrast of the halo display is linked to ice crystal shape, size, and surface roughness (Forster and Mayer, 2022).

Forward simulations with libRadtran

The library for radiative transfer libRadtran (Mayer and Kylling, 2005; Emde et al., 2016) was used for the radiative transfer calculations. The model calculates the radiative transfer through the Earth's atmosphere for different atmospheric conditions (Mayer and Kylling, 2005) based on the RTE (eq. 2.5).

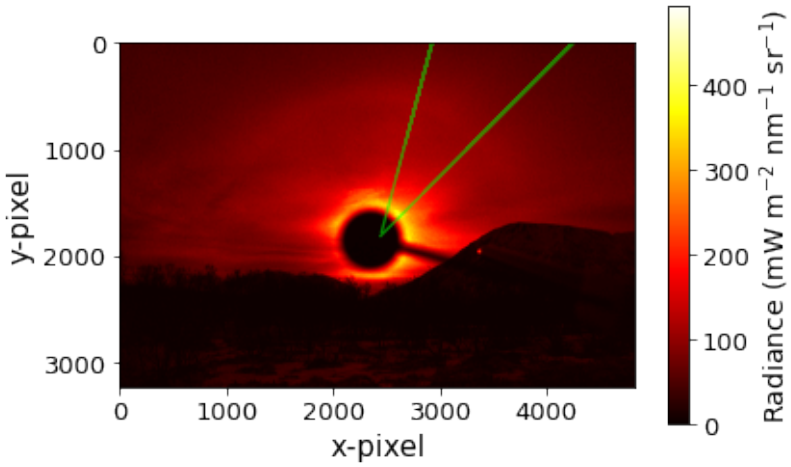

Figure 4.6: Radiance over the spectral wavelength range of the HaloCam red color channel. The two sold green lines represent the area of segment 4. Within this segment, the radiance was averaged over the scattering angle.

The atmospheric conditions can be implemented by the user and comprise, for instance, water and ice clouds, surface albedo, aerosols, solar angles, and profiles of temperature, humidity, and different gas species. Based on the atmospheric description, and optical properties, libRadtran includes a variety of solvers for the radiative transfer equation. For this thesis, the Discrete Ordinate Technique (DISORT) solver by Stamnes et al. (1988) was used to calculate the radiance distributions for different scattering angles. The DISORT solver computes radiance in plane-parallel geometry, based on discrete ordinates (Emde et al., 2016). This one-dimensional solver with pseudospherical geometry was chosen for the homogenous cirrus case to minimize the computational cost. We use the DISORT solver with the parameterizations from Yang et al. (2013) for the ice crystals optical properties. The scattering phase functions are provided for randomly oriented ice crystals for 9 different ice crystal habits. In addition, three degrees of ice crystal roughness are accounted for ranging from smooth, to moderately roughened, to severely roughened.

Initial conditions for libRadtran

Based on the location and time of measurement, the solar zenith angle (SZA) was set to 79.8° and the solar azimuth angle (SAA) to 10.1°. The surface albedo was set to 0.3 (snow-covered bushes, see Fig. 4.2). We assumed a

maritime, winter standard aerosol profile that was scaled to an AOD at 550 nm of 0.06. This value is based on measurements with a sunphotometer from an AERONET site close to the measurement location from February 2022 as it was not operational in February 2023. The spectral range was set to cover the spectral response of the camera ranging from 300 to 750 nm with a resolution of 5 nm. Hence, the simulations could be integrated over the red spectrum of the RSR function.

As the cirrus clouds were probed by the Romanian research aircraft before the halo image was taken, we based our estimates for the cirrus cloud in libRadtran mainly on those observations. Thus, the ice crystal effective radius was set to 70 μm. Based on the forecast in figure 4.4 (b) and the flight protocol, the cloud layer was placed at an altitude from 7-9 km. After some simplified test runs, the cloud optical thickness was assumed to be 0.7 to bring the simulated and observed radiance values within the same range. The radiance is then simulated for scattering angles ranging from 10° to 50° with a resolution of 0.1°.

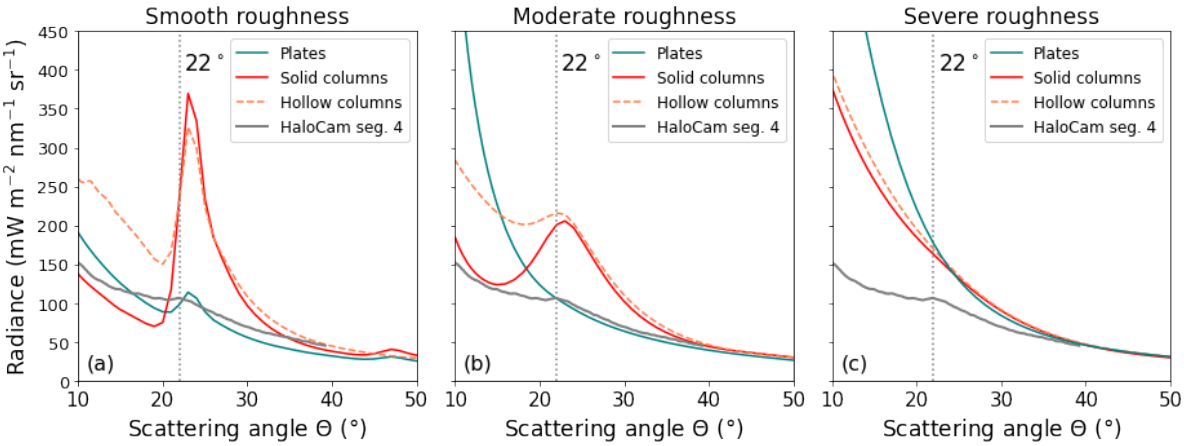

Figure 4.7: Radiance distributions observed by the HaloCam for segment 4 (solid grey line) and simulated by LibRadtran using the DISORT solver for different habits: plates (solid blue), solid columns (solid red), and hollow columns (dashed orange). The solver was implemented with an SZA of 79.8°. A cirrus layer at 7-9 km, with an optical thickness of 0.7, was implemented in the model. The effective radius of the ice crystals was set to 70 μm, and the optical properties of ice crystal from Yang et al., 2013 were used. (a) for smooth ice crystals, (b) for moderately roughened ice crystals, and (c) for severely roughened ice crystals. The 22° scattering angle is marked with a dotted grey line.

4.3 Ice crystal properties retrieval for Arctic cirrus case

Figure 4.7 shows the resulting simulated radiance distributions, together with the observed radiance from the HaloCam. The simulations cover ice crystal shapes that are capable of producing a 22° halo - plates, solid and hollow columns - for the 3 different roughness values. 4.7 (a) shows that the observed distribution is most similar to the distribution of smooth plates. The pathways are roughly equal, but the forward scattering peak at 22° is slightly overestimated. The distribution for solid and hollow columns has considerably higher 22° scattering peaks. These distributions have similar scattering peaks, but the radiance for hollow columns is larger by approximately 100 mW m^{-2} nm^{-1} sr^{-1} for scattering angles before the peak. The radiance distribution for solid columns is more similar to the ones for plates and the observed one before and after the scattering peak. In addition, the radiance distribution for plates and solid columns also indicates the presence of a 46° halo.

Figure 4.7 (b) shows the same observed radiance distribution, but the distributions for the different habits are simulated for moderately roughened ice crystals. With rougher ice crystals in the cirrus cloud, the 46° halo vanishes. Moreover, the 22° halo for moderately rough plates also vanishes. The moderately rough solid and hollow columns still produce a 22° halo, but the peak is overestimated by a large degree. The hollow columns still produce a higher radiance for scattering angles lower than the peak.

In accordance with figure 4.7 (c), the simulated 22° halo vanishes for all three habits when the ice crystals are severely roughened. The radiance at scattering angles less than 22° severely increases for all habits. This increase in radiance is largest for severely roughened plates.

CHAPTER 5

Discussion

In this chapter, the results of this thesis will be discussed. First, in section 5.1, the ice crystal properties, such as surface roughness and shape, in the cirrus cloud on 22 February 2023 as retrieved from HaloCam observations will be established. Then, in section 5.2 the limitations of the camera calibration and the methodology for characterizing ice crystal properties by comparing with radiative transfer simulations from the DISORT solver will be discussed. Finally, in section 5.3 the representativeness of cirrus cloud information obtained through halo observations for climate models will be discussed.

5.1 Information content of HaloCam observations

Based on the comparison between the observed and simulated radiance distributions in figure 4.7, the ice crystals likely had the shape of smooth hexagonal plates. This also fits when only looking at the observed distribution itself: the observed halo peak has a small halo ratio (HR, ratio between maximum and minimum of 22° halo), which is typical for plate-shaped ice crystals. The halo peaks for the simulations with solid and hollow columns have a considerably larger HR, which also suits this theory. In addition, the large difference of the 22° scattering peak can be explained by the fact that the 22° halo is produced by the refraction of solar radiation between two of the rectangular faces. Since the aspect ratio is higher for columns than for plates, the orientation of plate-shaped ice crystals needs to be accurate for the solar ray to be refracted between two of the rectangular faces.

Another point is that the 22° halo peak is only visible for smooth plates as

shown in figure 4.7. A study by Diedenhoven (2014) concluded that the fraction of smooth plate-shaped ice crystals must exceed 40% for a 22° halo to be visible. For column-shaped ice crystals, this fraction only amounts to 10% of the total ice crystals. This gives an indication that the smoothness of the plate-shaped ice crystals is a crucial property for a visible halo to appear. Moreover, the roughness of the ice crystals is known to decrease the forward scattering solar radiation (Forster, 2017). Since plate-shaped ice crystals have a lower HR, hence a lower brightness contrast to begin with, the increase of surface roughness will eliminate the halo faster.

Consequently, we conclude that (1) the simulated radiance distribution for smooth plates fits best to the observed distribution, and (2) that the properties behind the observed distribution itself fit for smooth plates. However, due to the collocation with the research aircraft, we can add another line of evidence. The aircraft was equipped with several in situ cloud probes, namely the SPEC Hawkeye and DMT CAPS. The Hawkeye Cloud Combination Probe can register cloud hydrometeors in a size range of 10 to 6,400 μm and consists, amongst others, of two perpendicularly aligned 2D-S probes that take stereo cloud particle images. Due to the fact that the MC^2 only recently finished, the post-processing of the cloud probe data is still ongoing. However, during the flight through the cirrus deck above Andenes on 22 February 2023, the mission scientist took a photo of the live view of the 2D-S probes (see Fig. 5.1). This confirms that the aircraft also found plate-shaped ice crystals in the cirrus cloud, in accordance with the retrieval from the HaloCam image. This gives us confidence that the halo photographs can be a representative measure of the ice crystal shape in Arctic cirrus clouds. However, it is clear that the closest simulated and observed radiance distributions are not exactly alike. The uncertainties and limitations of this methodology to retrieve ice crystal properties from halo photographs can explain some of these differences. This will be described in the next section.

A final point to be noticed is that the closest simulation for the observed radiance distribution also produces a 46° halo (see Fig. 4.7). Unfortunately, due to the field of view of the camera, a 46° halo will not be included in an image when the Sun is centered. This is also why the observed radiance curve ends at a scattering angle of about 40° for segment 4. For future halo observations,

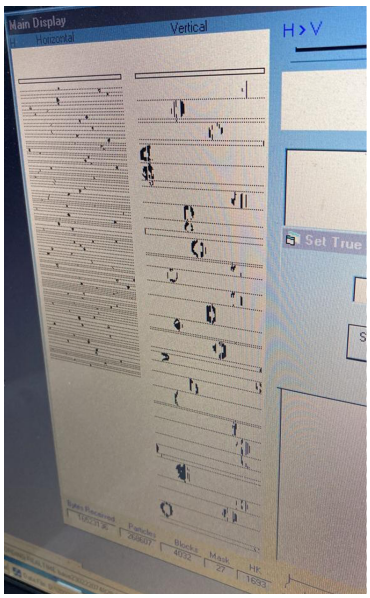

Figure 5.1: Photo of the live view of the 2D-S probes on 22 February 2023 taken by Robert O. David.

this finding can be taken into consideration, so the Sun position in the image can be adjusted according to the halo display.

5.2 Limitations of ice crystal properties retrieval

5.2.1 Uncertainty of HaloCam observations

Limitations in the accuracy of the HaloCam measurements are caused by uncertainties regarding the characterization and calibration of the camera.

The principal source of uncertainty for the radiometric calibration is linked to the calibrated output of the integrating sphere. For the calibration certificate used for the radiometric calibration, the relative uncertainty of the luminance is about 4% for the wavelength range of the red, green, and blue camera color channels.

The geometric calibration had several uncertainties. Foremost, the camera viewing zenith and azimuth angles were calculated for the pixels relative to the center pixel. This would be a valid method if the motive were mapped to the pixels perfectly. However, the spherical shape of the lens rather than

a more mathematically correct parabolic lens causes lens distortions (Bradski and Kaehler, 2008). This makes the pixels further away from the center to be distorted, creating a fish-eye-like effect. As the CVAA and CVZA were calculated for a perfect HaloCam lens, this causes the placement of the 22° halo to not entirely overlap with the captured halo on the image. On the other hand, the lens distortion is more present at the edges of the image, whereas the 22° halo is closer to the center (see Fig. 3.10 (b)). Moreover, the radiance distribution was calculated for 5 segments of the halo, making some of the segments more likely to overlap completely. In addition, information from some segments is more valuable, hence all segments are not necessarily needed. For example, the upper part of the 22° halo covered by the middle segment would also register a possible upper tangent arc. Thus, to only analyze the 22° halo, the surrounding segments are better suited.

As mentioned, due to the field of view of the camera, a 46° halo would not be captured by the camera when the sun is centered in the image. By tilting the camera such that the sun is localized on the lower part of the image, the upper part of a 46° halo is also possible to capture. For this purpose, the lens distortion definitely needs to be corrected, as the 46° halo would interact with the edges. Since the camera is not properly geometrically calibrated, as the distortion effect is not corrected, it is more accurate to describe the camera as geometrically characterized.

Another uncertainty concerning the HaloCam is that the picture was taken whilst operating the sun-tracker manually. Hence the sun was not completely centered in the image. The CVAA and CVZA were calculated from the center pixel, based on the assumption that the sun is centered in the image. To get the most accurate camera viewing angles, the center pixel was shifted towards the position of the sun. Yet, since the sun is not a point source (disc dimension) and blocked by the shader, the accurate position of the sun is hard to localize. Again, this can cause a slight misplacement of the 22° halo.

In addition, uncertainties attributed to the sensor characteristics are assumed to be small. A high linearity of the sensor and negligible dark current compared to the dynamical range of the sensor contribute little to the overall measurement

uncertainty. However, the overall uncertainty is hard to quantify mainly due to so-far uncorrected geometric effects. Nevertheless, this mainly influences the placement of the halo peak in the radiance distribution, but not the absolute value of the radiance itself, and has little implications for the retrieval applied to the Arctic cirrus case.

5.2.2 DISORT solver of the radiative transfer equation

The one-dimensional DISORT solver which solves the plane-parallel radiative transfer equation does not account for the spherical shape of the Earth, which requires three dimensions. This is computationally efficient, but can lead to inaccuracies at low Sun conditions. Forster and Mayer (2022) compared simulations of halo displays of the DISORT solver to a three-dimensional Monte Carlo solver for the physically correct tracing of photons in cloudy atmosphere (MYSTIC; Mayer, 2009; Emde and Mayer, 2007; Emde et al., 2010; Buras and Mayer, 2011; Emde et al., 2011). The resulting difference between the two solvers for a cirrus cloud at solar zenith angle at 50% was negligible. However, the solar zenith angle for Arctic latitudes can be much larger leading to a longer path of the photons through the atmosphere. Thus, multiple scattering effects in the atmosphere increase. With a larger amount of multiple scattering, the halo brightness contrast decreases (L. Forster et al., 2017). Since the DISORT solver does not account for this effect, the accuracy of the forward scattering peaks for solar radiation in the visible spectrum is limited (Mayer et al., 2020).

As mentioned, the solar zenith angle for the case study was roughly 80%. Thus, we ran the libRadtran simulations using disort in pseudo-spherical geometry. This uses a pseudo-spherical geometry for the direct part of the radiation and the plane-parallel geometry for the diffuse part of the radiation. This is more precise for the low Sun conditions encountered during the case study. However, differences between the pseud-spherical assumption and a rigorous spherical geometry still exist at such solar zenith angles (see libRadtran documentation).

5.3 Representativeness of HaloCam observations

HaloCam observations have a limited global coverage compared to spaceborne remote sensing. Since cirrus cloud properties vary over the globe, HaloCam observations are only representative of cirrus clouds in a specific region. However, spaceborne remote sensing has other limitations. For example, passive satellite methods struggle with detecting optically thin cirrus clouds, and with separating them from other clouds where ice dominates (Sassen et al., 2008). Moreover, halo displays give extra information on ice crystal shapes and surface roughness. This study focuses on Arctic cirrus clouds. Hence, such a study of cirrus clouds in a specific Arctic region can improve the representation of Arctic cirrus clouds in climate models. In that way, improving our understanding of regional variabilities in cirrus cloud properties is important to also improve their effects globally (Sassen and Campbell, 2001).

It should be emphasized that this study illustrates how HaloCam observations can be a valuable tool for retrieving information about ice crystal shape and surface roughness under Arctic low Sun conditions applying tools developed by L. Forster et al. (2017). For a complete study of ice crystal properties retrieved from halo displays, continuous long-term observations are necessary (L. Forster et al., 2017; Sassen et al., 2003). Additional information about ice crystal properties also requires further information on aerosol optical depth and cloud optical thickness to reduce degrees of freedom in the retrieval (Forster and Mayer, 2022). This can be achieved by collocated sunphotometer measurements.

CHAPTER 6

Summary, Conclusion, and Outlook

6.1 Summary and Conclusion

Cirrus clouds have the ability to produce various types of halo displays, which are determined by the size, shape, and orientation of ice crystals within the cloud. The objective of this thesis was to characterize and calibrate a digital camera for investigating ice crystal shapes in an Arctic cirrus cloud. The scattering properties of ice crystals contain essential information on ice crystal orientation, shape, size, and roughness. Knowledge of the scattering properties was achieved by analyzing the horizontally averaged radiance distribution with respect to the scattering angle. For this purpose, a digital camera was radiometrically and geometrically characterized and calibrated.

The characterization of the camera reveals: firstly, that the dark current is negligible and potentially independent of exposure time. Secondly, the signal for both the center and edge of the sensor is linearly dependent on exposure time, ISO number, and intensity of the incident radiation. Thirdly, the relative spectral response function (which is necessary to characterize for the radiometric calibration) has central wavelengths of 617, 546, and 477 nm with full widths at half maximum of 66, 124, and 76 nm for the red, green, and blue color channels, respectively.

The radiometric calibration of the camera establishes that the vignetting effect with darker pixels at the corners is clearly present. The vignetting effect is

slightly stronger for longer exposure times, which indicates that the degree of this effect is dependent on the overall amount of radiation that enters the system. The geometric calibration does not account for the lens distortion effect. Hence, this serves as a first-order approximation of the camera model. Because of this, the geometric calibration is more accurately described as a characterization of the camera. Due to the limited field of view of the camera, future analysis of a 46° halo can be executed for the upper halo part by tilting the camera.

The calibrated camera was applied to an Arctic cirrus case at Andenes, Norway, on 22 February 2023. When comparing the observed radiance distribution with forward simulations by the library for radiative transfer libRadtran using the DISORT solver, the ice crystals shape and roughness were obtained. In agreement with collocated airborne in-situ measurements, the cirrus cloud contained smooth hexagonal plate-shaped ice crystals.

The utilization of a calibrated camera for remote sensing of Arctic halo-producing cirrus clouds is shown to be a valuable tool for characterizing ice crystal properties even under low Sun conditions in the Arctic. Halo observations can thus be a relevant supplement to other techniques detecting ice crystal shapes and, ultimately, can help to improve estimates of the contribution of cirrus clouds to Arctic amplification.

6.2 Outlook

Further work regarding the remote sensing of Arctic halo displays with the HaloCam is needed to improve our understanding of Arctic ice crystal properties.

This thesis has focused on the common 22° halo produced by randomly oriented prism-shaped ice crystals. Still, there are multiple other types of halo displays as explained in section 2.3.1. Observations of upper and lower tangents arcs can give more details on oriented ice crystal columns. Oriented hexagonal plates can be characterized by sundog displays. Further studies regarding oriented ice crystals for Arctic cirrus clouds can give a broader view of Arctic ice crystal properties.

To limit the uncertainties of the camera measurements, the camera needs to be properly geometrically calibrated. For this, the lens distortion needs to be corrected. To correct this effect two different methods have been earlier described in L. Forster et al., 2017 and Carlsen, 2018. The first method includes taking several pictures of a check pattern while rotating and changing the placement of the camera. The second method involves stellar calibration, where images of stars with known positions are taken. For long-term observations of halo displays in the Arctic, such a calibration correcting for the lens distortion is needed.

Another improvement for long-term observations includes mounting the camera on an automated sun-tracking system. The tracking system allows the camera to move with the sun, by adapting the azimuth and elevation angle. The sun-tracker is crucial for long-term observation as:

1. Automatically observation of halo displays is retrieved.

2. The sun will always be centered (or positioned at a specific purposeful pixel position) in the image. This is a huge advantage when analyzing the images, as the camera viewing azimuth and zenith angles can be calculated from the center (chosen) pixel.

When performing long-term observations, the pictures that actually include halo displays need to be identified. As featured in L. Forster et al., 2017, a machine learning algorithm was developed for the detection of the 22° halo. A similar algorithm can be developed for long-term observation of Arctic halos, which also includes the detection of sundogs and upper and lower tangent arcs.

The calculation method for the radiative transfer simulations also needs to be improved for long-term observations. For this thesis, the input parameters for the radiative transfer simulations were based on the atmospheric conditions of the specific day of the case study. For analyzing several images for different days, pre-described look-up tables (LUTs) can be used to fit the measured radiance distributions. LUTs are generated for different solar zenith angles and geometric properties. Earlier studies from Forster and Mayer, 2022 generated

LUTs for solar zenith angles representative of mid-latitudes. These LUTs need to be extended to cover Arctic low Sun conditions.

LUTs can be created for different solvers of the radiative transfer equation. Since the DISORT solver does not account for the spherical shape of the earth, and the large multiple-scattering effect at a higher solar zenith angle, another solver could be a better fit for the Arctic. A three-dimensional solver that also calculates multiple-scattering effects due to the pathway of photons is the MYSTIC solver (Ma et al., 2017). Therefore, the MYSTIC solver can be an essential tool for calculating representative radiance distributions for the Arctic.

Overall, the main takeaways of this thesis for future observations with the HaloCam are:

1. Halo observations of upper and lower tangents arcs will provide a broader view of Arctic ice crystal properties.
2. The HaloCam needs to be properly geometrically calibrated correcting for the lens distortion effect.
3. Mounting the camera on an automated sun-tracking system is beneficial for long-term observations.
4. Implementation of an automatic halo detection algorithm is valuable for long-term observations.
5. Modification of radiative transfer simulations is required to account for Arctic low sun conditions.

Bibliography

Adobe (2023). *What is a RAW file and how do you open it? | Adobe*. en. URL: https://www.adobe.com/creativecloud/file-types/image/raw.html (visited on 29/03/2023).

Auriol, Frederique, Gayet, Jean-Franccois, Febvre, Guy, Jourdan, Olivier, Labonnote, Laurent and Brogniez, Gerard (Nov. 2001). 'In Situ Observation of Cirrus Scattering Phase Functions with 22° and 46° Halos: Cloud Field Study on 19 February 1998.' In: *Journal of the Atmospheric Sciences* vol. 58, pp. 3376–3390.

Baran, Anthony (Nov. 2004). 'On the scattering and absorption properties of cirrus cloud'. In: *Journal of Quantitative Spectroscopy and Radiative Transfer* vol. 89, pp. 17–36.

Bradski, Gary R. and Kaehler, Adrian (2008). *Learning OpenCV: computer vision with the OpenCV library*. en. 1. ed. United States of America: O'Reilly Media.

Buras, Robert and Mayer, Bernhard (Feb. 2011). 'Efficient unbiased variance reduction techniques for Monte Carlo simulations of radiative transfer in cloudy atmospheres: The solution'. en. In: *Journal of Quantitative Spectroscopy and Radiative Transfer* vol. 112, no. 3, pp. 434–447.

Cao, Hongtao, Gu, Xingfa, Wei, Xiangqin, Yu, Tao and Zhang, Haifeng (Jan. 2020). 'Lookup Table Approach for Radiometric Calibration of Miniaturized Multispectral Camera Mounted on an Unmanned Aerial Vehicle'. en. In: *Remote Sensing* vol. 12, no. 24, p. 4012.

Carlsen, Tim (2018). 'Influence of snow properties on directional surface reflectance in Antarctica'. Faculty of Physics and Earth Sciences. URL:

https://nbn-resolving.org/urn:nbn:de:bsz:15-qucosa2-319046. Phd thesis. Leipzig University.

Chandrasekhar, Subrahmanyan (Jan. 1960). *Radiative Transfer*. en. New York: Dover Publications.

Chylek, Petr, Folland, Chris, Klett, James D., Wang, Muyin, Hengartner, Nick, Lesins, Glen and Dubey, Manvendra K. (2022). 'Annual Mean Arctic Amplification 1970–2020: Observed and Simulated by CMIP6 Climate Models'. en. In: *Geophysical Research Letters* vol. 49, no. 13.

Coffin, Dave (2023). *Cyber Access Internet Communications, inc. web hosting, colocation, dialup internet access accounts in the boston, massachusetts area.* URL: http://www.cybercom.net/~dcoffin/dcraw/ (visited on 08/05/2023).

David, Robert O., Marcolli, Claudia, Fahrni, Jonas, Qiu, Yuqing, Perez Sirkin, Yamila A., Molinero, Valeria, Mahrt, Fabian, Brühwiler, Dominik, Lohmann, Ulrike and Kanji, Zamin A. (Apr. 2019). 'Pore condensation and freezing is responsible for ice formation below water saturation for porous particles'. In: *Proceedings of the National Academy of Sciences* vol. 116, no. 17, pp. 8184–8189.

De La Torre Castro, Elena et al. (Apr. 2023). 'Differences in microphysical properties of cirrus at high and mid-latitudes'. English. In: *EGUsphere*, pp. 1–34.

Diedenhoven, Bastiaan van (Oct. 2014). 'The prevalence of the 22° halo in cirrus clouds'. en. In: *Journal of Quantitative Spectroscopy and Radiative Transfer*. Electromagnetic and Light Scattering by Nonspherical Particles XIV vol. 146, pp. 475–479.

Dirik, Ahmet Emir and Karakucuk, Ahmet (Jan. 2014). 'Forensic use of photo response non-uniformity of imaging sensors and a counter method'. EN. In: *Optics Express* vol. 22, no. 1, pp. 470–482.

Emde, C., Buras, R., Mayer, B. and Blumthaler, M. (Jan. 2010). 'The impact of aerosols on polarized sky radiance: model development, validation, and applications'. English. In: *Atmospheric Chemistry and Physics* vol. 10, no. 2, pp. 383–396.

Emde, Claudia, Buras, Robert and Mayer, Bernhard (July 2011). 'ALIS: An efficient method to compute high spectral resolution polarized solar radiances

using the Monte Carlo approach'. en. In: *Journal of Quantitative Spectroscopy and Radiative Transfer* vol. 112, no. 10, pp. 1622–1631.

Emde, Claudia and Mayer, Bernhard (May 2007). 'Simulation of solar radiation during a total eclipse: a challenge for radiative transfer'. English. In: *Atmospheric Chemistry and Physics* vol. 7, no. 9, pp. 2259–2270.

Emde, Claudia et al. (May 2016). 'The libRadtran software package for radiative transfer calculations (version 2.0.1)'. en. In: *Geoscientific Model Development* vol. 9, no. 5, pp. 1647–1672.

Evers, Jeannie (May 2022). *Arctic*. en. URL: https://education.nationalgeographic.org/resource/arctic (visited on 27/04/2023).

Forster, Linda (2017). 'Information content of halo displays for remote sensing of ice crystal properties'. URL: https://edoc.ub.uni-muenchen.de/21811/. Phd thesis. Ludwig-Maximilians-Universität München.

Forster, Linda and Mayer, Bernhard (Nov. 2022). 'Ice crystal characterization in cirrus clouds III: retrieval of ice crystal shape and roughness from observations of halo displays'. English. In: *Atmospheric Chemistry and Physics* vol. 22, no. 23, pp. 15179–15205.

Forster, Linda, Seefeldner, Meinhard, Baumgartner, Andreas, Kölling, Tobias and Mayer, Bernhard (July 2020). 'Ice crystal characterization in cirrus clouds II: radiometric characterization of HaloCam for the quantitative analysis of halo displays'. English. In: *Atmospheric Measurement Techniques* vol. 13, no. 7, pp. 3977–3991.

Forster, Linda, Seefeldner, Meinhard, Wiegner, Matthias and Mayer, Bernhard (July 2017). 'Ice crystal characterization in cirrus clouds: a sun-tracking camera system and automated detection algorithm for halo displays'. English. In: *Atmospheric Measurement Techniques* vol. 10, no. 7, pp. 2499–2516.

Forster, Piers et al. (2021). 'The Earth's energy budget, climate feedbacks, and climate sensitivity'. In: *Climate Change 2021: The Physical Science Basis. Contribution of Working Group I to the Sixth Assessment Report of the Intergovernmental Panel on Climate Change*. Ed. by Masson-Delmotte, Valérie et al. Cambridge, United Kingdom and New York, NY, USA: Cambridge University Press, pp. 923–1054.

Gedzelman, S. D. (Jan. 2003). 'OPTICS, ATMOSPHERIC | Optical Phenomena'. en. In: *Encyclopedia of Atmospheric Sciences*. Ed. by Holton, James R. Oxford: Academic Press, pp. 1583–1594.

Guignard, A., Stubenrauch, C. J., Baran, A. J. and Armante, R. (Jan. 2012). 'Bulk microphysical properties of semi-transparent cirrus from AIRS: a six year global climatology and statistical analysis in synergy with geometrical profiling data from CloudSat-CALIPSO'. en. In: *Atmospheric Chemistry and Physics* vol. 12, no. 1, pp. 503–525.

Heymsfield, Andrew J. et al. (Jan. 2017). 'Cirrus Clouds'. en. In: *Meteorological Monographs* vol. 58, no. 1. Publisher: American Meteorological Society Section: Meteorological Monographs, pp. 2.1–2.26.

Kanji, Zamin A., Ladino, Luis A., Wex, Heike, Boose, Yvonne, Burkert-Kohn, Monika, Cziczo, Daniel J. and Krämer, Martina (Jan. 2017). 'Overview of Ice Nucleating Particles'. en. In: *Meteorological Monographs* vol. 58, no. 1, pp. 1.1–1.33.

Keim, Robert (2020). *Introduction to Image Sensor Technology, from Photons to Electrons - Technical Articles*. en. URL: https://www.allaboutcircuits.com/technical-articles/introduction-to-image-sensor-technology-photons-to-electrons/ (visited on 08/05/2023).

Kokhanovsky, Alexander and Tomasi, Claudio (2020). *Physics and Chemistry of the Arctic Atmosphere*. en. 1st ed. Springer Polar Sciences. 6330 Cham, Switzerland: Springer Nature Switzerland AG.

Korolev, A. V., Isaac, G. A. and Hallett, J. (1999). 'Ice particle habits in Arctic clouds'. en. In: *Geophysical Research Letters* vol. 26, no. 9, pp. 1299–1302.

Korolev, Alexei and Leisner, Thomas (Oct. 2020). 'Review of experimental studies of secondary ice production'. English. In: *Atmospheric Chemistry and Physics* vol. 20, no. 20, pp. 11767–11797.

Krämer, Martina et al. (Mar. 2016). 'A microphysics guide to cirrus clouds – Part 1: Cirrus types'. en. In: *Atmospheric Chemistry and Physics* vol. 16, no. 5, pp. 3463–3483.

Kärcher, B. (July 2005). 'Supersaturation, dehydration, and denitrification in Arctic cirrus'. English. In: *Atmospheric Chemistry and Physics* vol. 5, no. 7, pp. 1757–1772.

Kärcher, Bernd (May 2018). 'Formation and radiative forcing of contrail cirrus'. en. In: *Nature Communications* vol. 9, no. 1, p. 1824.

Lamb, Dennis and Verlinde, Johannes (2011). *Physics and Chemistry of Clouds*. Cambridge: Cambridge University Press.

Li, Haoran (Jan. 2021). 'Growth and Melting of Atmospheric Ice Particles: Insights from Radar Observations'. PhD thesis. University of Helsinki.

Liou, Kuo-Nan and Yang, Ping (Sept. 2016). *Light Scattering by Ice Crystals: Fundamentals and Applications*. en. 1st ed. Cambridge University Press.

Ma, Yuzhao, Liu, Wenrong, Cui, Yafeng and Xiong, Xinglong (Aug. 2017). 'Multiple-scattering effects of atmosphere aerosols on light-transmission measurements'. en. In: *Optical Review* vol. 24, no. 4, pp. 590–599.

Mayer, B, Kylling, A, Emde, C, Hamann, U, Buras, R, Gasteiger, J and Richter, B (2020). 'libRadtran User's Guide'. en. In: version 2.0.4.

Mayer, B. and Kylling, A. (July 2005). 'Technical note: The libRadtran software package for radiative transfer calculations - description and examples of use'. English. In: *Atmospheric Chemistry and Physics* vol. 5, no. 7, pp. 1855–1877.

Mayer, Bernhard (2009). 'Radiative transfer in the cloudy atmosphere'. en. In: *EPJ Web of Conferences* vol. 1, pp. 75–99.

Meredith, Michael et al. (2019). 'Polar Regions'. en. In: *IPCC Special Report on the Ocean and Cryosphere in a Changing Climate*. Cambridge, UK and New York, NY, USA, Cambridge University Press, pp. 203–320.

metoffice.gov.uk (2023). *Weather and climate change - Met Office*. URL: https://www.metoffice.gov.uk/ (visited on 11/05/2023).

Minnis, Patrick, Garber, Donald P., Young, David F., Arduini, Robert F. and Takano, Yoshihide (Nov. 1998). 'Parameterizations of Reflectance and Effective Emittance for Satellite Remote Sensing of Cloud Properties'. EN. In: *Journal of the Atmospheric Sciences* vol. 55, no. 22, pp. 3313–3339.

Murphy, D. M. and Koop, T. (2005). 'Review of the vapour pressures of ice and supercooled water for atmospheric applications'. en. In: *Quarterly Journal of the Royal Meteorological Society* vol. 131, no. 608, pp. 1539–1565.

NASA (Aug. 2022). *Clouds & Their Impact on Global Warming*. en. URL: https://mynasadata.larc.nasa.gov/lesson-plans/clouds-their-impact-global-warming (visited on 07/05/2023).

Noel, Vincent, Chepfer, Helene, Haeffelin, Martial and Morille, Yohann (Nov. 2006). 'Classification of Ice Crystal Shapes in Midlatitude Ice Clouds from Three Years of Lidar Observations over the SIRTA Observatory'. EN. In: *Journal of the Atmospheric Sciences* vol. 63, no. 11, pp. 2978–2991.

Oxford Instruments (2023). *Understanding Read Noise in sCMOS Cameras*. en. URL: https://andor.oxinst.com/learning/view/article/understanding-read-noise-in-scmos-cameras (visited on 14/04/2023).

Rensselaer Polytechnic Institute (2004). *Spectral Response | Photosensors Tutorial | Specifier Report | NLPIP | LRC*. URL: https://www.lrc.rpi.edu/programs/nlpip/tutorials/photosensors/spectral.asp (visited on 17/04/2023).

Rogers, R. R. and Yau, Man Kong (1989). *A short course in cloud physics*. eng. 3rd ed. Vol. 113. International series in natural philosophy. Oxford: Pergamon Press.

Sassen, Kenneth and Campbell, James R. (Mar. 2001). 'A Midlatitude Cirrus Cloud Climatology from the Facility for Atmospheric Remote Sensing. Part I: Macrophysical and Synoptic Properties'. en. In: *Journal of the Atmospheric Sciences* vol. 58, no. 5, pp. 481–496.

Sassen, Kenneth, Wang, Zhien and Liu, Dong (2008). 'Global distribution of cirrus clouds from CloudSat/Cloud-Aerosol Lidar and Infrared Pathfinder Satellite Observations (CALIPSO) measurements'. en. In: *Journal of Geophysical Research: Atmospheres* vol. 113, no. D8.

Sassen, Kenneth, Zhu, Jiang and Benson, Sally (Feb. 2003). 'Midlatitude Cirrus Cloud Climatology from the Facility for Atmospheric Remote Sensing. IV. Optical Displays'. In: *Applied optics* vol. 42, pp. 332–41.

Schäfer, Britta, Carlsen, Tim, Hanssen, Ingrid, Gausa, Michael and Storelvmo, Trude (July 2022). 'Observations of cold-cloud properties in the Norwegian Arctic using ground-based and spaceborne lidar'. English. In: *Atmospheric Chemistry and Physics* vol. 22, no. 14, pp. 9537–9551.

Selek, Murat (Jan. 2016). 'A New Autofocusing Method Based on Brightness and Contrast for Color Cameras'. In: *Advances in Electrical and Computer Engineering* vol. 16, pp. 39–44.

SONY (Mar. 2021). *What is the difference between Exmor and Exmor R sensors? | Sony USA*. URL: https://www.sony.com/electronics/support/articles/00070962 (visited on 28/03/2023).

Stamnes, Knut, Tsay, S.-Chee, Wiscombe, Warren and Jayaweera, Kolf (June 1988). 'Numerically stable algorithm for discrete-ordinate-method radiative transfer in multiple scattering and emitting layered media'. en. In: *Applied Optics* vol. 27, no. 12, pp. 2502–2509.

Taylor, Patrick C. et al. (2022). 'Process Drivers, Inter-Model Spread, and the Path Forward: A Review of Amplified Arctic Warming'. In: *Frontiers in Earth Science* vol. 9.

Teledyne Photometrics (2023). *Dark Current - Learn*. en-US. URL: https://www.photometrics.com/learn/advanced-imaging/dark-current (visited on 30/03/2023).

Thomas, Gary E. and Stamnes, Knut (1999). *Radiative Transfer in the Atmosphere and Ocean*. Cambridge Atmospheric and Space Science Series. Cambridge: Cambridge University Press.

Wallace, John M. and Hobbs, Peter V. (2006). *Atmospheric science: an introductory survey*. eng. 2nd ed. Vol. vol. 92. International geophysics series. Amsterdam: Elsevier.

Wang, Hong, Yang, Jianfeng and Xue, Bin (Sept. 2020). 'A novel method for the definition of central wavelength and spectral bandwidth'. en. In: *Results in Physics* vol. 18, p. 103327.

Wang, Pao K. (2013). *Physics and Dynamics of Clouds and Precipitation*. Cambridge: Cambridge University Press.

Warren, Stephen G. and Brandt, Richard E. (July 2008). 'Optical constants of ice from the ultraviolet to the microwave: A revised compilation'. en. In: *Journal of Geophysical Research* vol. 113, no. D14, p. D14220.

Wendisch, Manfred and Yang, Ping (2012). *Theory of Atmospheric Radiative Transfer - A Comprehensive Introduction*. en. Weinheim, Germany: Wiley-VCH Verlag GmbH & Co. KGaA.

WMO (2017). *Cirrus (Ci)*. EN. URL: https://cloudatlas.wmo.int/cirrus-ci.html (visited on 13/04/2023).

Yang, Ping, Bi, Lei, Baum, Bryan A., Liou, Kuo-Nan, Kattawar, George W., Mishchenko, Michael I. and Cole, Benjamin (Jan. 2013). 'Spectrally Consistent Scattering, Absorption, and Polarization Properties of Atmospheric Ice Crystals at Wavelengths from 0.2 to 100 m'. en. In: *Journal of the Atmospheric Sciences* vol. 70, no. 1, pp. 330–347.

Zelinka, Mark D., Myers, Timothy A., McCoy, Daniel T., Po-Chedley, Stephen, Caldwell, Peter M., Ceppi, Paulo, Klein, Stephen A. and Taylor, Karl E. (2020). 'Causes of Higher Climate Sensitivity in CMIP6 Models'. en. In: *Geophysical Research Letters* vol. 47, no. 1.

Zinkova, Mila (2018). 'Ice halos in weather lore and meteorology, and a rare halo display in San Francisco'. en. In: *Weather* vol. 73, no. 8, pp. 239–246.